Characterizing long-period seismic effects of long-wavelength elastic and anelastic models

Joseph S. Resovsky and Michael H. Ritzwoller
University of Colorado, Department of Physics, Campus Box 390, Boulder, CO 80309-0390, USA

SUMMARY

We present the results of a synthetic investigation designed to characterize the effects of long-wavelength elastic and anelastic models on the amplitudes and phases of long-period normal mode multiplets and Rayleigh wavepackets. Normal mode synthetics are created for recently constructed long-wavelength elastic and anelastic aspherical models of the Earth's upper mantle, using both the multiplet self-coupling approximation and the more accurate ±5 multiplet–multiplet coupling of the Galerkin method. Amplitude and phase measurements of the normal mode spectral peaks between 2 and 9 mHz and of the first eight Rayleigh wavepackets for 331 source–receiver pairs are compiled for each type of synthetic. The effects of anelastic and elastic structures are compared quantitatively with one another and with the predictions of zeroth order (in $1/l$) asymptotic normal mode theory and linearized ray theory (LRT), and difficulties and advantages of applying these theoretical simplifications are identified and discussed.

Although anelastic structures have only a minor effect on phases, long-wavelength models of anelastic and elastic structure each perturb amplitude measurements, with anelasticity accounting for up to ~1/3 of the normal mode perturbations and up to ~1/2 of the surface wave amplitude effect. Zeroth-order asymptotic theory and LRT predict that elastic and anelastic amplitude effects should qualitatively differ from one another, and thus should be separable in the data. While synthetics display qualitative agreement with the predictions of the approximations, for both normal mode spectra and surface wave measurements significant quantitative departures from zeroth-order asymptotic theory and LRT are observed. The part of the synthetic elastic amplitude signal not forecast by the approximate theories obscures the effects of aspherical anelasticity, particularly for normal modes, and can severely bias estimates of anelastic structure based solely on the approximations.

In contrast, if an *a priori* model of aspherical elastic structure is assumed, the transfer functions that map amplitude anomalies from the elastic model to those for a model which includes anelastic asphericity are much more accurately forecast by zeroth-order asymptotic theory and LRT. Asymptotic theory accounts for over 85 per cent of the variance of such transfer functions for normal modes, and LRT predicts 67 per cent of the variance of surface wave transfer functions. Therefore, with the assumption of *a priori* elastic models, or in joint inversions of amplitude and phase data for elastic and anelastic structure, the approximations considered should prove useful for estimating models of aspherical attenuation.

Key words: aspherical structure, asymptotic approximations, Q, ray theory, synthetic seismograms.

1 INTRODUCTION

In recent years, the first models of long-wavelength anelasticity in the Earth's upper mantle have emerged (Ritzwoller, Durek & Woodhouse 1989; Romanowicz 1990; Durek, Ritzwoller & Woodhouse 1993) to be added to earlier long-wavelength elastic models (e.g. Woodhouse & Dziewonski 1984; Tanimoto 1986; Smith & Masters 1989; Romanowicz 1991). Renewed theoretical interest in the seismic effects of anelasticity has also occurred in the past

few years (Tromp & Dahlen 1990; Lognonné 1991). This recent progress motivates our investigation, which seeks to quantify the relative effects of long-wavelength elastic and anelastic structures in long-period seismic data, in order to provide a basis for judging the viability of employing certain approximate mathematical methods in the development of future models.

It is well known that long-period seismic amplitude anomalies result from elastic as well as anelastic aspherical structures (e.g. Jobert & Roult 1976; Davis 1985; Park 1986; Woodhouse & Wong 1986; Pollitz, Park & Dahlen 1987). Durek *et al.* (1993) discussed at length how long-wavelength elastic asphericities bias estimated anelastic models, under certain assumptions. They addressed this problem by using an elastic reference model to reduce the elastic amplitude contamination, but argued that eventually a simultaneous inversion for elastic and anelastic structures would be necessary. Even simultaneous inversions would need to be informed as to the relative effects of elastic and anelastic structures in order to resolve ambiguities resulting from the analysis of data that are affected by elastic and anelastic structures similarly. However, though studies have been published that quantify the phase signal in long-period seismic data resulting from long-wavelength elastic structure (e.g. Davis & Henson 1986), we are unaware of any similar study that concentrates on the amplitudes of the long-wavelength models, elastic or anelastic.

The studies that produced the anelastic models, cited above, analysed amplitude anomalies of multiply orbiting Rayleigh wavepackets and were each based on a number of simplifying assumptions which were used to extract the anelastic amplitude signal from the larger elastic signal. These assumptions, in turn, were derived from linearized or asymptotic approximations in the theoretical representation of normal mode and surface wave seismograms. We wish to describe the effects and limitations of these approximations and to display more concretely the particular contributions of anelasticity. Just as the description of the lowest and first-order asymptotic effects of elastic structure permitted Romanowicz, Roult & Kohl (1987) to isolate zeroth-order effects in phase data, improved understanding of the anelastic signal may indicate means of isolating particular information about attenuative structure in the data, advancing the work of Romanowicz (1990) and Durek *et al.* (1993).

There are, therefore, three main purposes to this study.

(1) To quantify the relative size of the long-period signal of long-wavelength aspherical anelastic and elastic models with a particular emphasis on amplitudes.

(2) An attempt to quantify the degree to which linearized and asymptotic approximations are successful in predicting the characteristics of the anelastic signal, since these methods speed inversion.

(3) To interpret our results in terms of their implications for the development of future inversions for general aspherical Earth structure.

2 SYNTHETIC SEISMOGRAMS AND MODELS

2.1 Methods

To construct synthetics using sums of coupled normal modes, we start with a set of vector eigenfunctions of

oscillation, $s_K(r)$, for a spherical, non-rotating, elastic, isotropic (SNRI) earth model. The index K represents the radial, angular, and azimuthal indices (n, l, m) of a spherical harmonic eigenfunction and r is the position vector. The coupled normal mode formulism can then be simply stated as follows.

In the spectral neighbourhood of fiducial frequency ω_0, the displacement field $d(t)$ at position r due to an event at r_s is given by (e.g. Woodhouse & Girnius 1982):

$$d(r, t) = R^* \cdot \exp{(iZt)} \cdot S \exp{(i\omega_0 t)}. \tag{1}$$

The receiver vector R is composed of the projections on to the receiver's polarization axis of the eigenfunctions $s_K(r)$ evaluated at position r, while the source vector S comprises the moment tensor contracted with the complex conjugate of the strain tensors of the basis functions evaluated at r_s. Ignoring boundary contributions, the functional dependence on aspherical structure is contained in the general matrix Z, the elements of which describe coupling between pairs of basis functions and can be written as (Woodhouse 1980):

$$Z_{nn'll'}^{mm'} = [(\omega_{nl}^2 - \omega_0^2)\delta_{nn'} + C_{nn'l}^m]\delta_{ll'}\delta_{mm'}$$
$$+ \sum_{s,t} \gamma_{ll's} \begin{pmatrix} l' & s & l \\ -m' & t & m \end{pmatrix} \begin{pmatrix} l' & s & l \\ 0 & 0 & 0 \end{pmatrix} c_{s(nn'll')}^t, \tag{2}$$

where ω_{nl} is the degenerate frequency of each multiplet, $C_{nn'l}^m$ represents terms in the Coriolis force and centripetal acceleration, $\gamma_{ll's} = [(2l+1)(2l'+1)(2s+1)/(4\pi)]^{1/2}$, and the Wigner 3-j symbols multiply the interaction or structure coefficients which are linearly related to aspherical structure:

$$c_{s(nn'll')}^t = \int_0^a \delta m_s^t(r) \cdot K_{s(nn'll')}(r) r^2 \, dr. \tag{3}$$

The model vector is $\delta m_s^t = (\delta \kappa_s^t, \delta \mu_s^t, \rho_s^t, q_s^t)$ where s and t are the spherical harmonic degree and order of the aspherical structure. The kernel K is also a vector, with components corresponding to those of δm, and is a function of the SNRI eigenvectors.

The general matrix Z is diagonalized to yield the perturbed eigenfrequencies and eigenfunctions of the aspherical model:

$$Z = U \cdot \Omega \cdot U^{-1}. \tag{4}$$

The elements of U are the coefficients in the expansion of the perturbed eigenfunctions in the basis of SNRI eigenfunctions, and the diagonal components of Ω are the frequency perturbations that give the new eigenfrequencies. The displacement can be rewritten

$$d(r, t) = \mathscr{R}^* \cdot \exp{(i\Omega t)} \cdot \mathscr{S} \exp{(i\omega_0 t)}, \tag{5}$$

where $\mathscr{R}^* = R^* \cdot U$ and $\mathscr{S} = U^{-1} \cdot S$. For our purposes the infinite dimension of the general matrix is reduced to a manageable size by assuming that the modes of each degenerate SNRI multiplet couple only to singlets in that multiplet and to those of its nearest neighbours along the fundamental ($n = 0$) mode branch. As described by Park (1986), we find the perturbed modes of a 'target' multiplet by constructing the coupling matrix that includes the P (a small integer) multiplets on either side of the target. We solve the eigenvalue problem for the central block of this matrix to retrieve the perturbed modes and frequencies of the target. This process is repeated for each multiplet along

a section of the fundamental branch to produce the modes summed for a $\pm P$ coupled synthetic.

Our own tests as well as several other studies (e.g. Park 1986; Masters 1989; Um, Dahlen & Park 1991) have shown that, for long-wavelength upper mantle models, coupling to modes beyond ± 5 alters spectra only slightly compared with the effects of coupling within that limit. We have, therefore, chosen to construct ± 5 coupled synthetics for this experiment. Even so, the computation time required for the diagonalization of matrices corresponding to modes with frequencies greater than 9 mHz has proven to be prohibitive. Our limited range of frequencies is sufficient to display important characteristics of the signal of aspherical anelasticity in surface waves, including significant deviations from the predictions of asymptotic approximations and linearized ray theory. However, in further experiments it should be possible to extend the frequency range upward using the more efficient subspace projection technique (Dahlen 1987; Park 1987), as well as asymptotic methods based on the work of Romanowicz (1987) and Snieder (1986).

2.2 Models

The chosen spherically symmetrical reference model is the Preliminary Reference Earth Model (PREM) of Dziewonski & Anderson (1981). The aspherical elastic model is a hybrid. We have combined the lower mantle v_p model LO2.56 (Dziewonski 1984), the upper mantle v_s model for degrees 1–8 given by M84A (Woodhouse & Dziewonski 1984), and the degree 9–12 part of MPA12.4A (Wong 1989). (The degree 1–8 part of Wong's model does not differ greatly from M84A, and the combination is used for historical reasons only.) We translate all models into the form $\delta \ln v_s(r, \theta, \phi)$, employing the lower mantle scaling relation $d(\ln v_s)/d(\ln v_p) = 2.0$.

For the model of aspherical anelasticity, we draw on the results of Durek et al. (1993), who inverted their estimated surface wave attenuation coefficients for a 3-D attenuation model using the radially dependent proportionality coefficient $\alpha(r)$, which maps aspherical velocity perturbations into perturbations in intrinsic anelasticity q $(=1/Q)$ according to:

$$\delta q_\mu(r, \theta, \phi) \equiv \alpha(r)\delta \ln v_s(r, \theta, \phi). \qquad (6)$$

This assumption reflects the likelihood that variations in attenuation are dominantly controlled by temperature, which has larger gradients in the radial than in the lateral directions. The resulting function $\alpha(r)$ (Fig. 1a) displays a source region for anelastic heterogeneity located in and just below the low-velocity zone of PREM, consistent with the postulate that material in this zone is near, but below, the solidus temperature (Sato, Sacks, & Murase 1989a; Sato et al. 1989b). The scale and geometry of the lateral variations in the attenuation model at the base of the low-velocity zone are displayed in Fig. 1(b).

2.3 Synthetic data sets

We consider four different types of synthetic seismograms, which we define according to the earth model and normal mode coupling scheme used to construct them. The earth models we consider are composed of PREM alone or

PREM combined with the aspherical elastic and/or anelastic models described above (four possible combinations). The coupling schemes are self-coupling or ± 5 coupling. Of the seven types of synthetics that can be constructed with these models and coupling schemes, we select for this investigation the following: PREM modes perturbed only by rotation and ellipticity; PREM and the aspherical elastic model under self-coupling; PREM and the aspherical elastic model under ± 5 coupling; and PREM, the aspherical elastic, and the aspherical anelastic models under ± 5 coupling. Hereafter, we will refer to these synthetics respectively as RH (rotating hydrostatic), elastic self, elastic ± 5, and anelastic ± 5 synthetics. Note that 'anelastic ± 5' synthetics include *both* elastic and anelastic aspherical earth models. Consequently, this sequence, summarized in Table 1, is presented in order of increasingly realistic approximations to seismograms of a complete earth model.

For each type of synthetic seismogram, we create a set of vertical component synthetics for 331 source–receiver pairs, which have been selected in such a way that great circle poles are well distributed across the Earth's surface (Fig. 2). The 24 events are from 1977 through 1984, with locations and moment tensors from the Harvard CMT catalogues. The receivers are IDA and GDSN stations that were in place during that period.

We do not consider here the additional, undoubtedly important, effects that smaller scale structures would have on the low-frequency spectrum. We further restrict this investigation to an analysis of Rayleigh waves. The effects of toroidal–toroidal coupling are seen only in Love waves, while spheroidal–toroidal coupling is primarily attributable to the Earth's rotation and anisotropy (Park & Yu 1992; Yu & Park 1993), which are beyond the scope of this study. Thus, our concentration on anelasticity and Rayleigh waves necessitates only the construction of coupled-mode synthetics for fundamental $(n = 0)$ spheroidal modes.

3 PERTURBATIONS IN FUNDAMENTAL MODE SPECTRA

3.1 Measurements

Amplitude and phase spectra are computed by taking the Fourier transform of the first 15 hr of the Hanning windowed synthetic time series. Motivated by the predictions of asymptotic theory, summarized by eq. (A19), we measure the amplitude of multiplets at their peaks, and phases at the degenerate frequencies of the unperturbed multiplets. For each type of synthetic considered, and for each of the 331 source–receiver pairs selected, these measurements are made on all of the multiplets in the range $l = 20$ to $l = 85$.

3.2 Observations

We consider the amplitude and phase changes that occur as we switch from one type of synthetic method and/or model to the next, and compare, in succession, elastic self to RH, elastic ± 5 to elastic self, and anelastic ± 5 to elastic ± 5. In each case we record, for every multiplet of the synthetics for each path, the phase shift $\phi' - \phi$ and the relative amplitude shift $\delta A/A$, where $A' = A + \delta A$, and primes indicate the perturbed values. Measurements near nodes are ignored in this process. Though such measurements provide unique
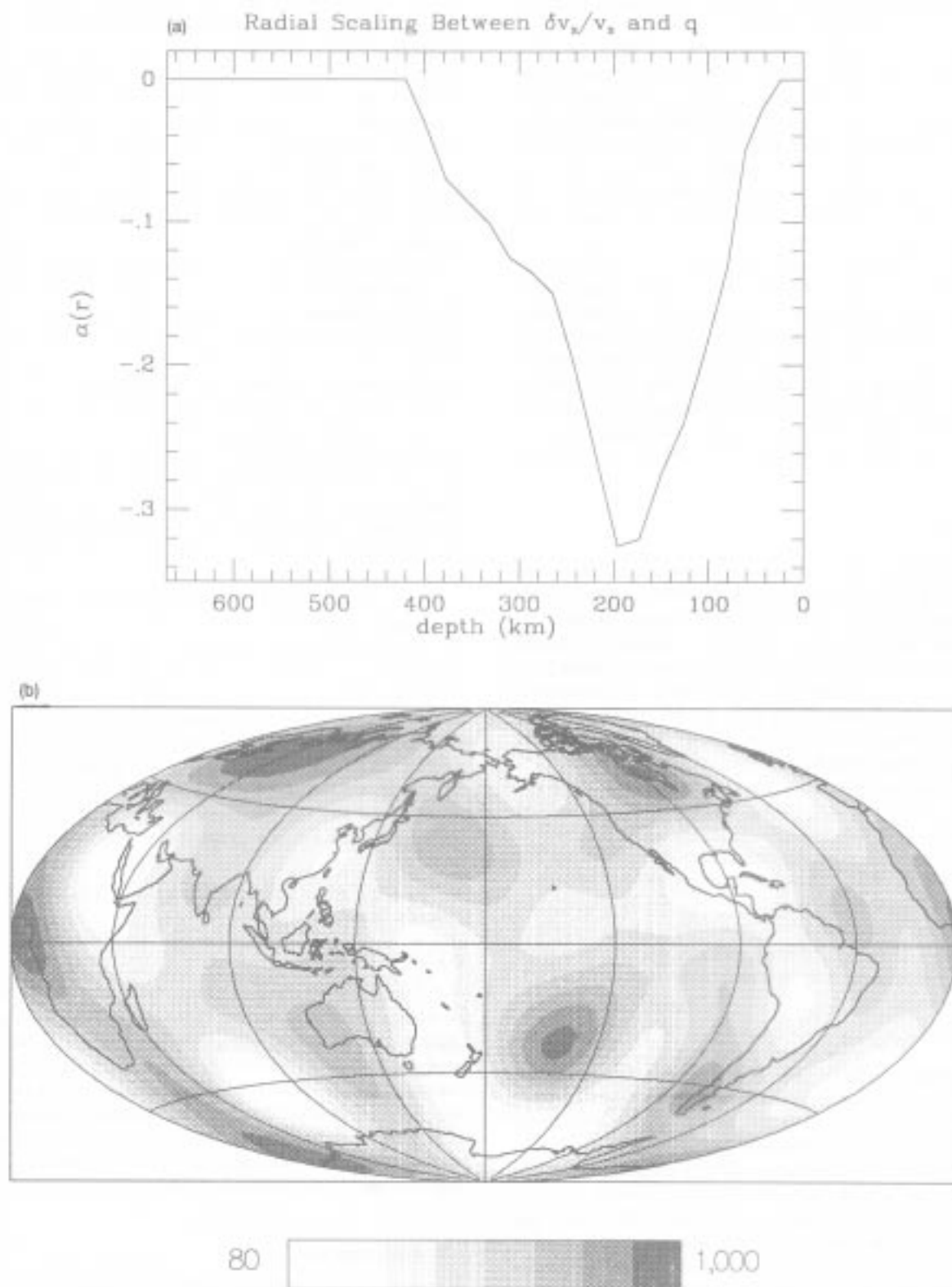
Figure 1. (a) The proportionality constant $a(r)$ between relative perturbations of shear velocity and anelasticity in the upper mantle (eq. 1), as estimated by Durek *et al.* (1993). Note that the negative peak is at the base of the low-velocity zone at 200 km depth. (b) The lateral Q model at 200 km implied by eq. (6), the model of $a(r)$ in (a), and the aspherical elastic model M84A. The shading scale at the bottom of the figure indicates Q values, while the contour lines are those of $q = Q^{-1}$. Note that there are high Q anomalies under the continental shields and the old Pacific, and low Q regions beneath the East African rift system and the Caribbean, among other places.

Table 1. Identification of synthetic seismograms according to the earth models and normal mode coupling schemes employed. PREM is the Preliminary Reference Earth Model (Dziewonski & Anderson 1981); the aspherical elastic model is a combination of LO2.56 (Dziewonski 1984), M84A (Woodhouse & Dziewonski 1984), and MPA12.4A (Wong 1989); the anelastic model is derived, using eq. (1), from the model of $\alpha(r)$ shown in Fig. 1 and the aspherical elastic model. Self-coupling implies that normal modes are allowed to couple only to other modes of the same harmonic degree (same degenerate multiplet), while ±5 coupling allows both self-coupling and coupling to modes of the 10 nearest neighbouring multiplets on the fundamental mode branch.

synthetic designation	Earth model	coupling type
RH	PREM	self
elastic self	PREM + asph. elas.	self
elastic ±5	PREM + asph. elas.	±5
anelastic ±5	PREM + asph. elas. + asph. anel.	±5

and important information, peaks with near zero amplitude in the RH model spectra skew the amplitude ratio statistics that we focus on here.

Figure 3 displays the straight average of the absolute value of amplitude and phase perturbations, for the set of 331 source–receiver pairs. The amplitudes of the elastic self-coupling synthetics are perturbed from those of the RH synthetics by about 7 per cent throughout the range of harmonic degrees displayed. These perturbations are attributable to phase interference among singlets in each multiplet, a second-order phenomenon that is essentially independent of harmonic degree in the frequency range examined here.

The inclusion of coupling terms produces additional perturbations that increase in magnitude from 5 per cent at $l = 20$ to 20 per cent at $l = 85$. Elastic coupling is, then, the strongest contributor to the amplitude signal, but the amplitude shift produced by our long-wavelength anelastic model relative to the elastic ±5 synthetics becomes increasingly significant with greater harmonic degree. For the highest frequency multiplets considered, the relative amplitude perturbation due to anelasticity is nearly 10 per cent, which is more than one-third of the total average perturbation due to long-wavelength structure at those frequencies.

In contrast, the average phase difference between multiplets of the anelastic ±5 and elastic ±5 synthetics is at most 2 degrees, while the difference in phases between the RH synthetics and elastic self-coupling synthetics ranges from 25 to 60 degrees, and the difference between the elastic self and elastic ±5 phases is up to 20 degrees. The strongest phase signal from our earth model results, therefore, from elasticity through self-coupling, while the phase effect of long-wavelength anelastic structure is negligible, being near the noise level of real data.

In order to gain a better understanding of the nature of the amplitude signal of anelastic structure in normal mode amplitudes, we examime in greater detail a pair of synthetic seismograms corresponding to different ranges (Δ) along great circle paths, which sample predominantly high or low Q regions of the anelastic model. The paths selected for this

inspection are shown in Fig. 4, and Figs 5 and 6 display portions of synthetic spectra for the high and low Q paths, respectively.

Figures 5(a) and 6(a) show the spectra for the elastic self and elastic ±5 synthetics. The amplitude perturbations of the ±5 synthetic relative to the corresponding self-coupling synthetic for the high Q path increase in magnitude with harmonic degree. Both spectra and the pattern of perturbations in each are all dominated by an oscillating function of l with a period very near 2. For the low Q path similar effects are seen, but in this case the dominant oscillating function describing the perturbations has a period slightly greater than 2.

These effects are better illustrated by plotting the *transfer function*

$$T^{\rm NM}_{\rm self \to \pm 5}(l) = A^{(\pm 5)}_{\rm elas}(l)/A^{(\rm self)}_{\rm elas}(l), \tag{7}$$

which maps normal mode (NM) amplitudes of elastic self-coupling synthetics to elastic ±5 amplitudes. $T^{\rm NM}_{\rm self \to \pm 5}$ for the low Q path is plotted in Fig. 7(a). Any smooth trend in the perturbations is clearly dominated by the oscillating function. The periods observed here correspond to those given by the function $\tan(k\Delta - \pi/4)$, with $k = l + 1/2$, derived in Davis & Henson (1986) and Romanowicz & Roult (1986), among others, and appearing in Appendix A. This function gives l-periods of 2.05 and 1.89 for the $\Delta = 88°$ and $\Delta = 95°$ paths, respectively. The period 1.89 gets mapped to the observed period of 2.12 by the Nyquist effect of once-per-multiplet sampling.

Figs 5(b) and 6(b) display the spectra of the elastic ±5 and anelastic ±5 synthetics. The effect of the long-wavelength attenuation model is primarily to increase all modal amplitudes for the high Q path and decrease them all for the low Q path. The magnitude of this anelastic amplitude shift increases with harmonic degree, and there are periodic fluctuations similar to, but significantly smaller than, those observed in the upper plots for the effect of elastic coupling.

We consider next the transfer function

$$T^{\rm NM}_{\rm c \to a}(l) = A^{(\pm 5)}_{\rm anel}(l)/A^{(\pm 5)}_{\rm clas}(l), \tag{8}$$

which characterizes the effect of adding aspherical anelasticity to the aspherical elastic earth model. The transfer functions for the high and low Q paths are shown as dotted lines in Fig. 7(b). In contrast with $T^{\rm NM}_{\rm self \to \pm 5}$, these functions are dominated by trends that vary smoothly with l, on which are superimposed smaller scale oscillations of roughly constant periodicity. This result is closely analogous to the elastic frequency perturbations described by Davis & Henson (1986).

Also plotted in Fig. 7(b) are lines that are derived from the term of order zero in $(1/l)$ of the asymptotic theory described in Appendix A (eq. A20). The analytic expression for these lines is approximately (eq. A24)

$$T^{\rm theory}_{\rm c \to a}(l) = 1 + \frac{\delta \hat{Q}_l}{Q_l}, \tag{9}$$

which is derived by generalizing the equations of Romanowicz (1987) to include aspherical attenuative structure. Q_k is the quality factor of the multiplet for PREM. $\delta \hat{Q}_k$ is the average of aspherical Q along a great
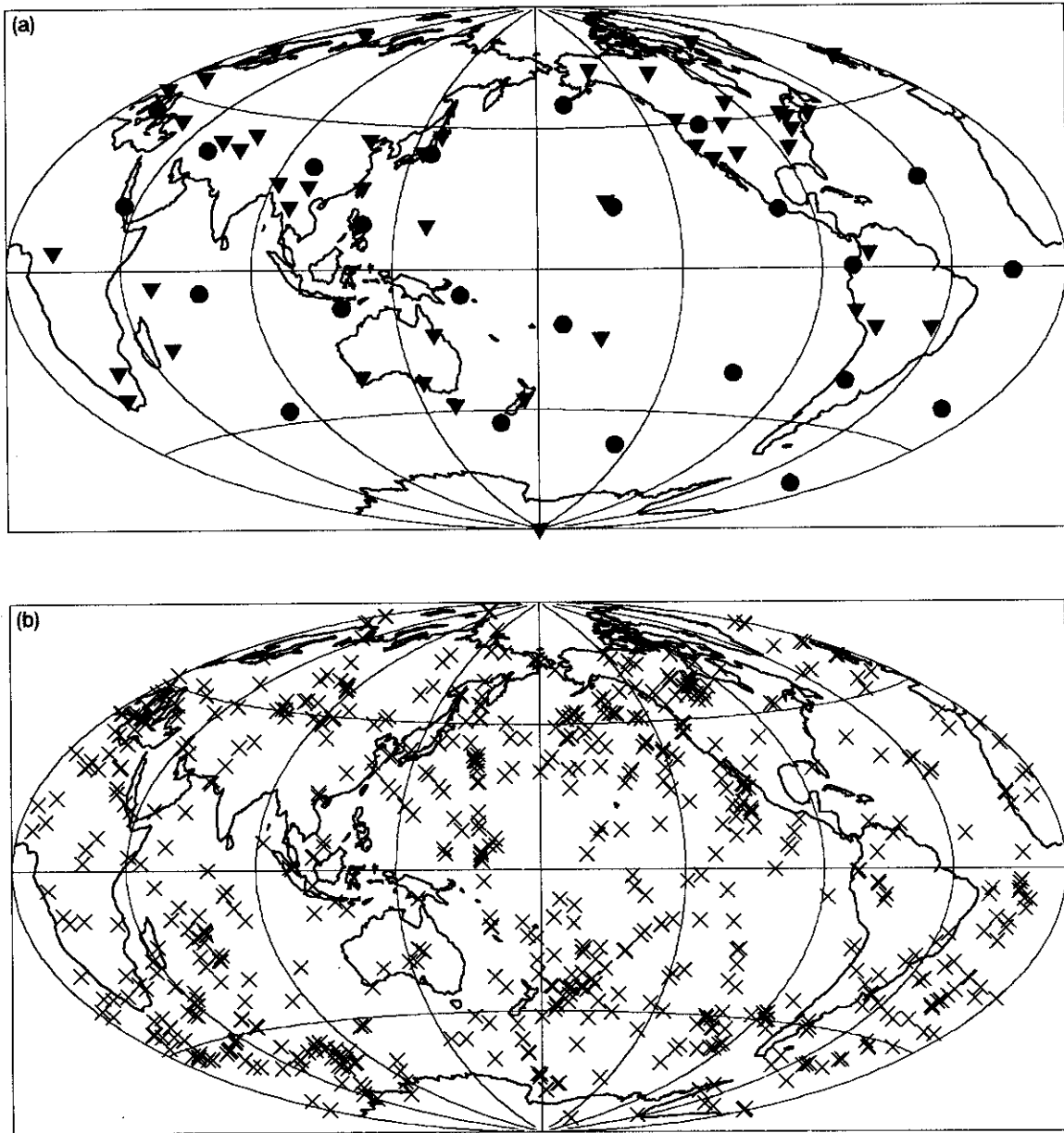
Figure 2. (a) The 24 events from 1977 to 1984 (circles) and 49 IDA and GDSN receivers (triangles) used for this synthetic investigation. (b) Great circle poles for the 331 source–receiver paths of the synthetics created. Note that great circle poles are fairly well distributed across the Earth's surface.

circle linking source and receiver, depth sampled according to the sensitivity kernel of the specified multiplet. To the extent that asymptotic theory is correct, eq. (9), with corrections to account for the effects of tapering the time series, should match the smooth trend of the measured amplitude perturbations. Mismatches, such as those visible in Fig. 7(b), are attributable to the inaccuracy of the short-time approximations of asymptotic theory when frequency perturbations are large. We postpone to Section 3.3 discussion of the predictions of the asymptotic theory and the degree to which the observations for this model agree with those predictions.

To illustrate further the general nature of $T_{e \to a}^{NM}$, transfer functions for the suite the paths shown in Fig. 8 have been plotted in Fig. 9. Again we see that the large-scale trends

are smoothly varying and appear to be fairly simple. There are visible periodic oscillations in these trends, and careful inspection reveals that the periodicity for each path corresponds to that of $\tan(k\Delta - \pi/4)$. We display the plots in order of increasing path-averaged Q perturbation, $\delta\hat{Q}$, and it is evident that for this suite of paths the approximate slope of the transfer functions is positively correlated with $\delta\hat{Q}$, as suggested by eq. (9).

3.3 Discussion

3.3.1 Theoretical expectations

A generalization of the results of Romanowicz (1987) to include anelasticity may be found in Appendix A1. The
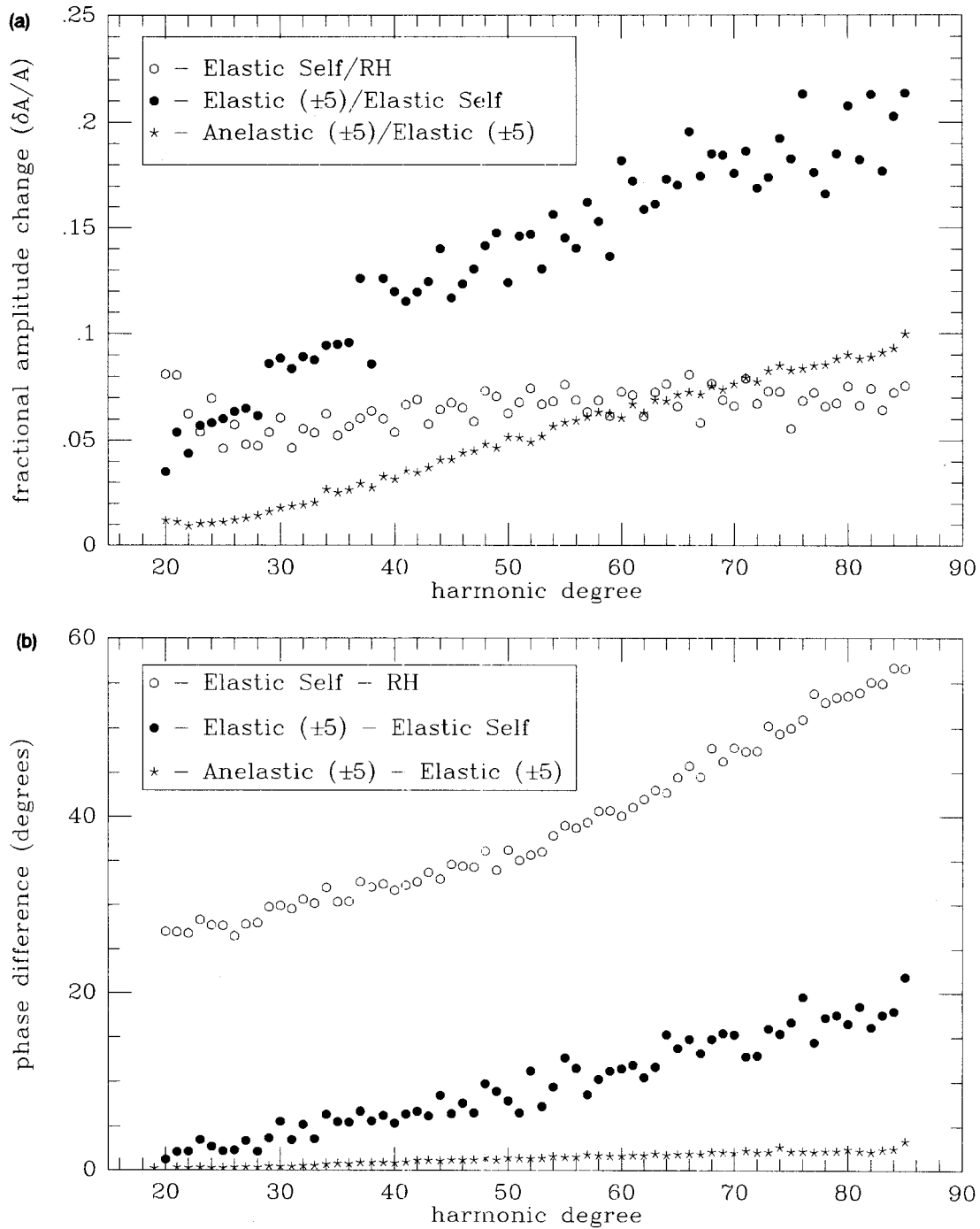
Figure 3. (a) Fractional amplitude differences as functions of harmonic degree (*l*). Plotted for each harmonic degree is the average of the magnitude of ($\delta A/A$) that results from a comparison of multiplet peak amplitudes. A separate trend is displayed for each of three types of synthetic ratios (as defined in the text): elastic self to RH (open circles); elastic ±5 to elastic self (solid circles); anelastic ±5 to elastic ±5 (stars). (b) Average phase differences for the same synthetic pairs represented in (a). Phases are measured at the degenerate multiplet peak frequencies of the SNRI model synthetics.

relevant results of this asymptotic theory are summarized by expressions for the amplitude, phase and frequency perturbations caused by aspherical structure. These equations are correct to the first order in $(1/l)$ and all are based on the short-time approximation, $\Lambda T \ll 1$, for a frequency shift Λ and a time series of length T.

The asymptotic equation for the perturbed time series in the case of an isotropic source in an earth model with both elastic and anelastic asphericities is

$$s(t, \Delta) = \Re e \left[\sum_k a_k (A_{0k} + \delta A_k) \exp\left[-(\alpha_k + \delta\alpha_k)t\right] \right.$$

$$\left. \times \exp\left\{i[(\omega_k + \Lambda_k)t + \psi_k^{\text{anel}}]\right\} \right], \tag{10}$$
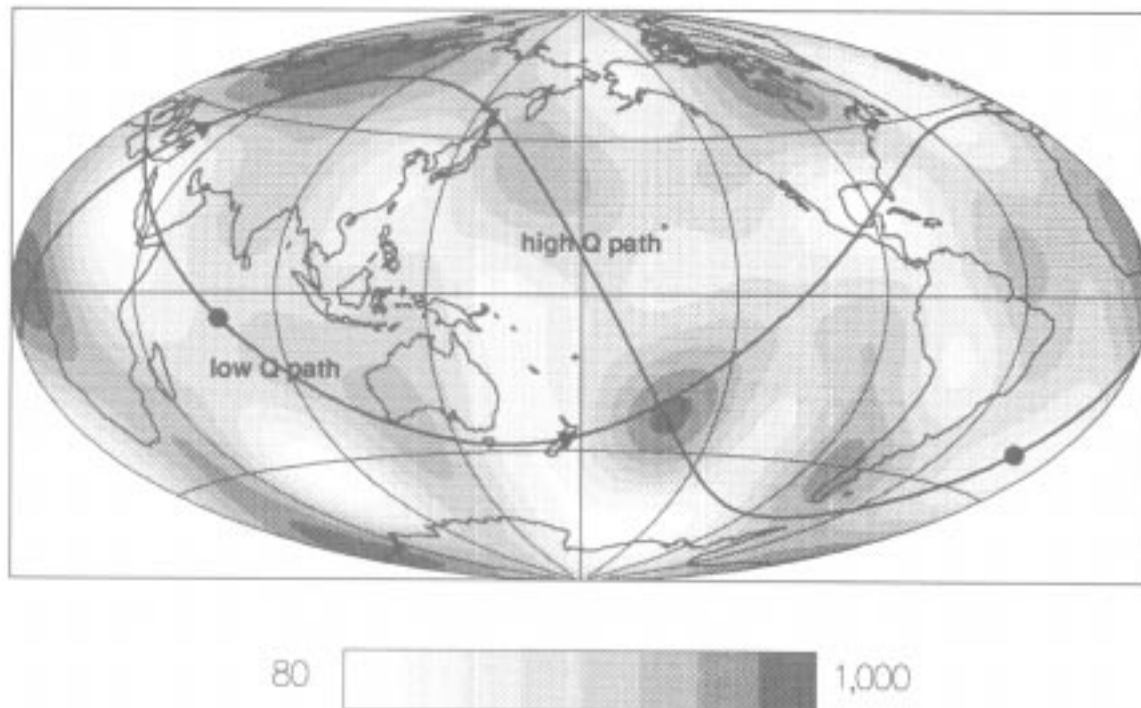
Figure 4. Two complementary paths, plotted on the Q model at depth 200 km. The high Q path ($\delta\hat{Q} = 10.68$ for $l = 50$) passes through the Asian shield and the old Pacific, and is tangent to structural contours in North Africa, where gradients are large. The low Q path ($\delta\hat{Q} = -7.92$ for $l = 50$) passes through the East African rift and the Caribbean, and is roughly orthogonal to contours almost everywhere. The high Q path is for the Indian Ocean event of 1983 November 30 recorded at the South Karori, New Zealand GDSN station (SNZO). The low Q path is for the South Atlantic ridge event of 1981 June 3 recorded at the Ankara, Turkey GDSN station (ANTO).

where $\alpha_k = \omega_k/2Q_k$ is the attenuation coefficient of the unperturbed multiplet with wavenumber k. The predicted frequency shift produced by aspherical elastic structure is given by

$$\Lambda_k = \delta\hat{\omega}_k + \frac{\bar{D}_k}{2k}\tan\lambda_k. \tag{11}$$

Laterally varying elastic structure also changes the amplitudes of multiplets, and the amplitude perturbation relative to the amplitudes produced by the RH model is

$$\frac{\delta A_k}{A_{0k}} = \frac{a\Delta}{U_k}\left(-\overline{\delta\omega}_k\tan\lambda_k + \frac{\bar{D}_k}{2k} + \frac{\cot\Delta}{8k}\overline{\delta\omega}_k\sec^2\lambda_k\right). \tag{12}$$

U_k is the group velocity at frequency ω_k, and $\lambda_k = k\Delta - \pi/4$ for range Δ. $\delta\hat{\omega}_k$ is the average, along the source–receiver great circle path, of the local frequency $\delta\omega(\theta, \phi)$ defined by Woodhouse & Girnius (1982). This local frequency is a radial integral of the variations in elastic structural parameters introduced by an aspherical model. $\hat{D}$ is similarly the great circle average of $D(\theta, \phi)$, which depends on the gradient of $\delta\omega$ in the direction transverse to the great circle. $\overline{\delta\omega}$ and $\bar{D}_k$ stand for the differences between great circle and minor arc averages of $\delta\omega$ and D. $\delta\hat{\omega}_k$ and $\hat{D}$ result from the self-coupling terms of the general matrix $\mathbf{Z}$, while $\overline{\delta\omega}$ and $\bar{D}_k$ come from coupling between different multiplets.

To first-order in $(1/l)$, asymptotic theory predicts that the elastic phase shift results from self-coupling alone, and that

the amplitude perturbations caused by elastic asphericity are produced entirely by coupling between multiplets, according to eq. (12). Much of this study will focus on amplitude measurements, and we see that the strongest part of the amplitude signal of aspherical elastic structure is expected to take the form of a periodic function of l, due primarily to the zeroth-order term in eq. (12), though the contribution of the oscillating first-order term of the same periodicity can be strong for some paths. Departures from simple periodicity due to the smooth first-order gradient term in eq. (12) are expected to be significant, because bending of surface waves in the same frequency range, attributable to gradients of elastic structure, has been observed. Higher order asymptotic effects may also be observable in synthetic amplitude data. Additionally, non-asymptotic amplitude effects may be significant for paths with large average local frequency, $\delta\hat{\omega}$, giving frequency perturbations, Λ, large enough to violate the short-time approximation for the 15 hr time series of this experiment. For example, at $l = 75$ the frequency perturbation for the high Q path is 0.023 mHz, for which $\Lambda T \approx 0.5$ when $T = 1$ hr. In this case, then, the assumption $\Lambda T \ll 1$ is valid only for time series well less than 1 hr in length.

Because laterally varying attenuative structures produce perturbations to the imaginary part of the local frequency, the predictions of the asymptotic theory for the amplitude and phase signals of anelastic asphericity match, respectively, the expressions for the frequency and amplitude perturbations due to elastic structure. The attenuation coefficient of a multiplet is perturbed, again to the first order
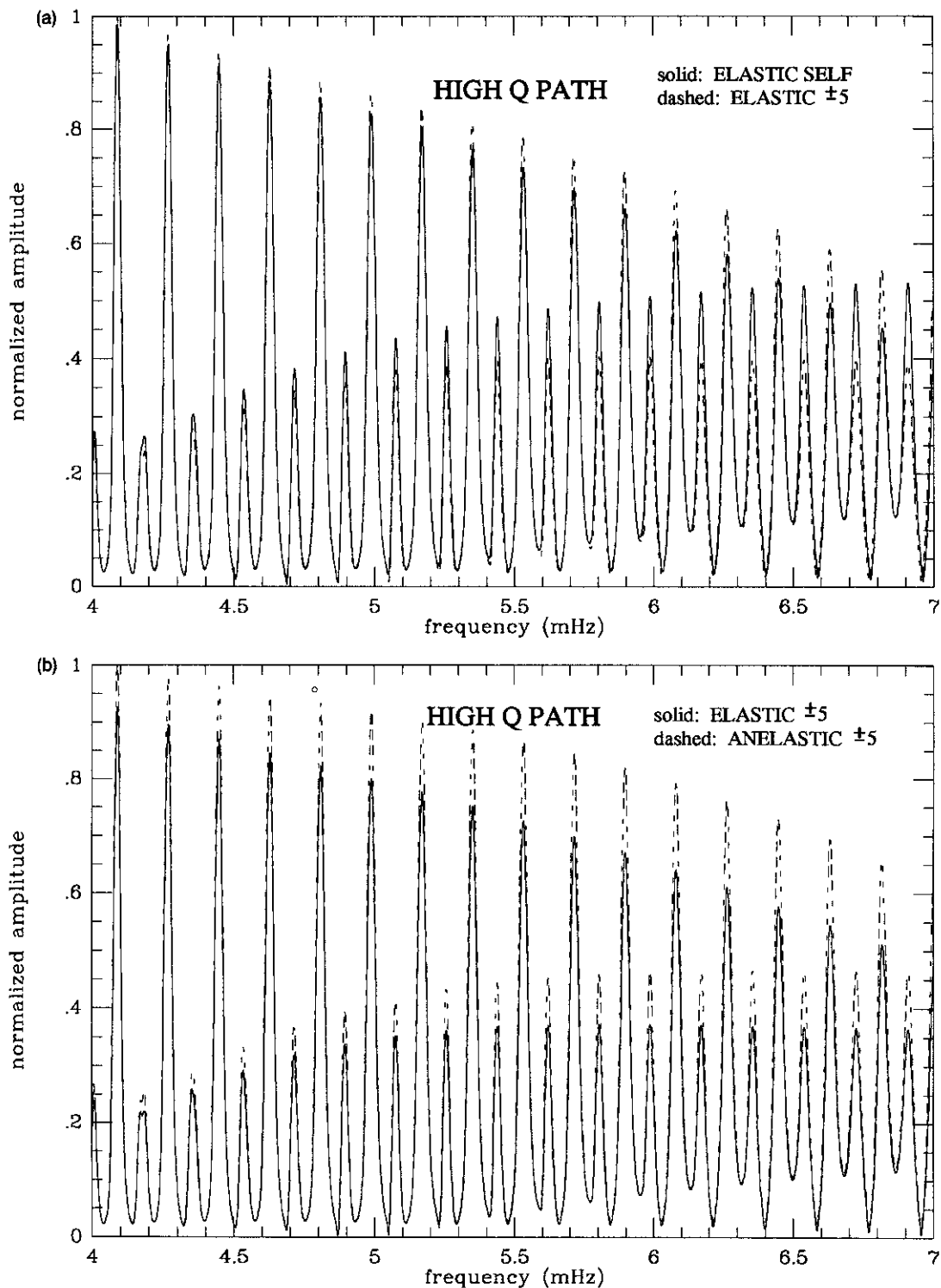
Figure 5. Normal mode spectra for the high Q path displaying the amplitude signals of elastic and anelastic aspherical structures. In (a) a portion of the spectrum resulting from a self-coupling synthetic for the aspherical elastic earth model is compared with that from the ± 5 coupled synthetic for the same model. The latter, plotted as a dashed line in (a) becomes the solid 'reference' spectrum of (b) where it is compared with the spectrum of the ± 5 coupled synthetic for the model with both elastic and anelastic lateral structure. The dominant effect of elastic coupling is seen to be a periodic pattern of positive and negative amplitude shifts, while anomalously high aspherical Q structure predominantly increases all amplitudes.
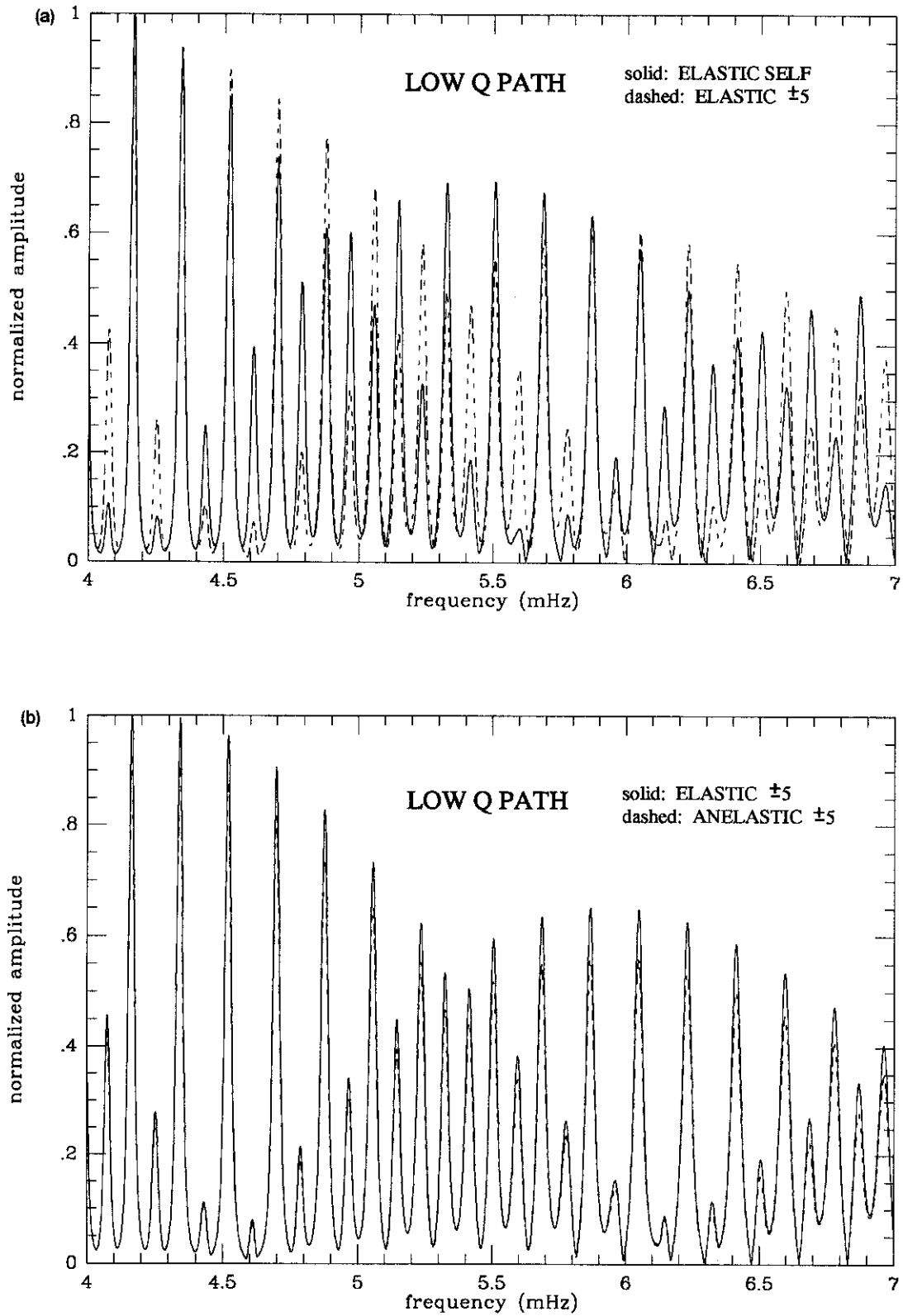
(a)

(b)

Figure 6. Same as Fig. 5, but for the low Q path. In this case, the primary effect of low Q structure is seen to be a downward shift of the entire amplitude spectrum.
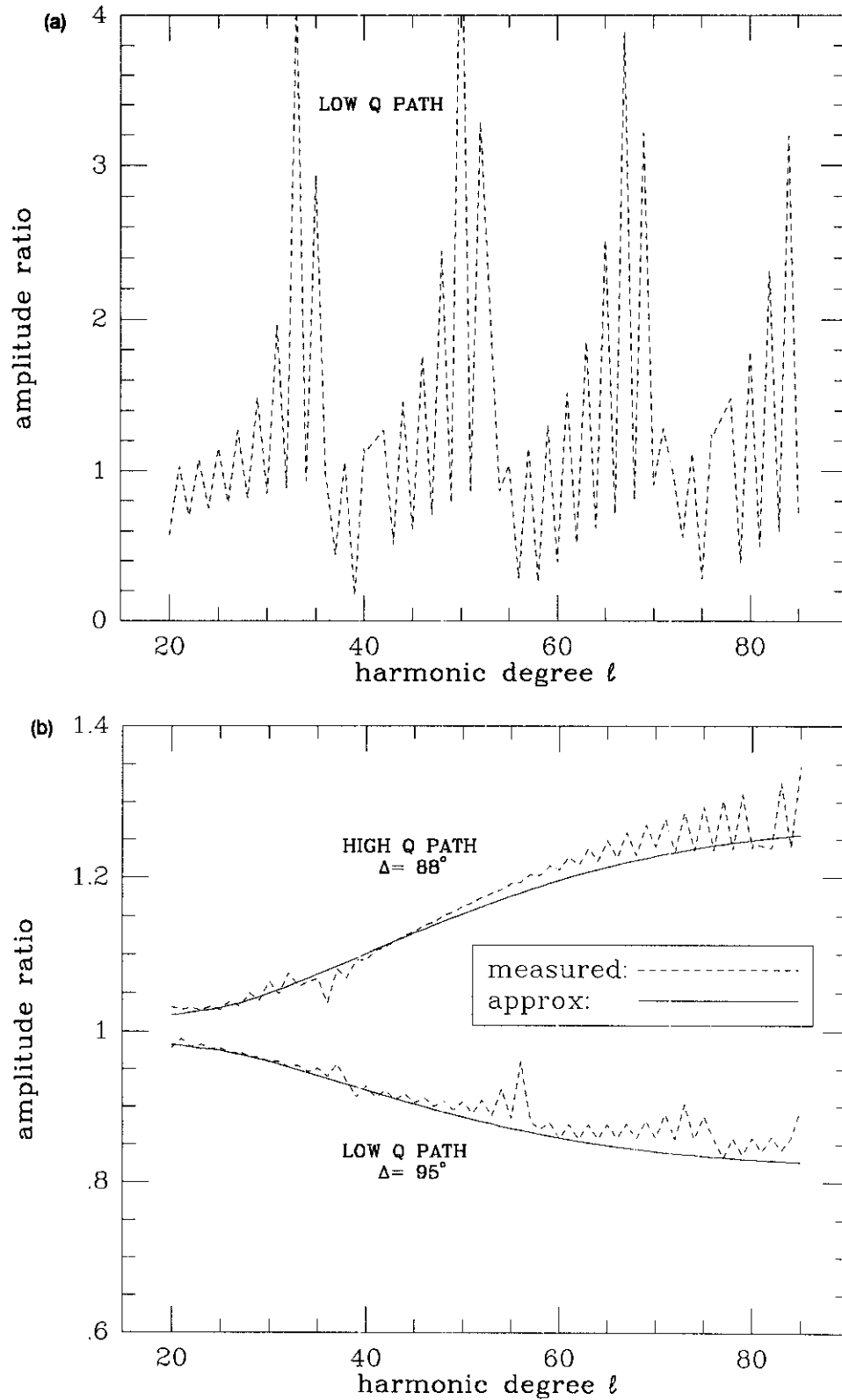
Figure 7. Normal mode transfer functions. (a) The transfer function $T^{NM}_{self \rightarrow \pm 5}(l)$ for the low Q path. Note that amplitudes are changed by more than a factor of 4 in some cases. (b) Transfer functions $T^{NM}_{c \rightarrow a}(l)$. For comparison, the theoretical lines for zeroth-order (in $1/l$) asymptotic theory, given by eq. (A28), are also plotted.
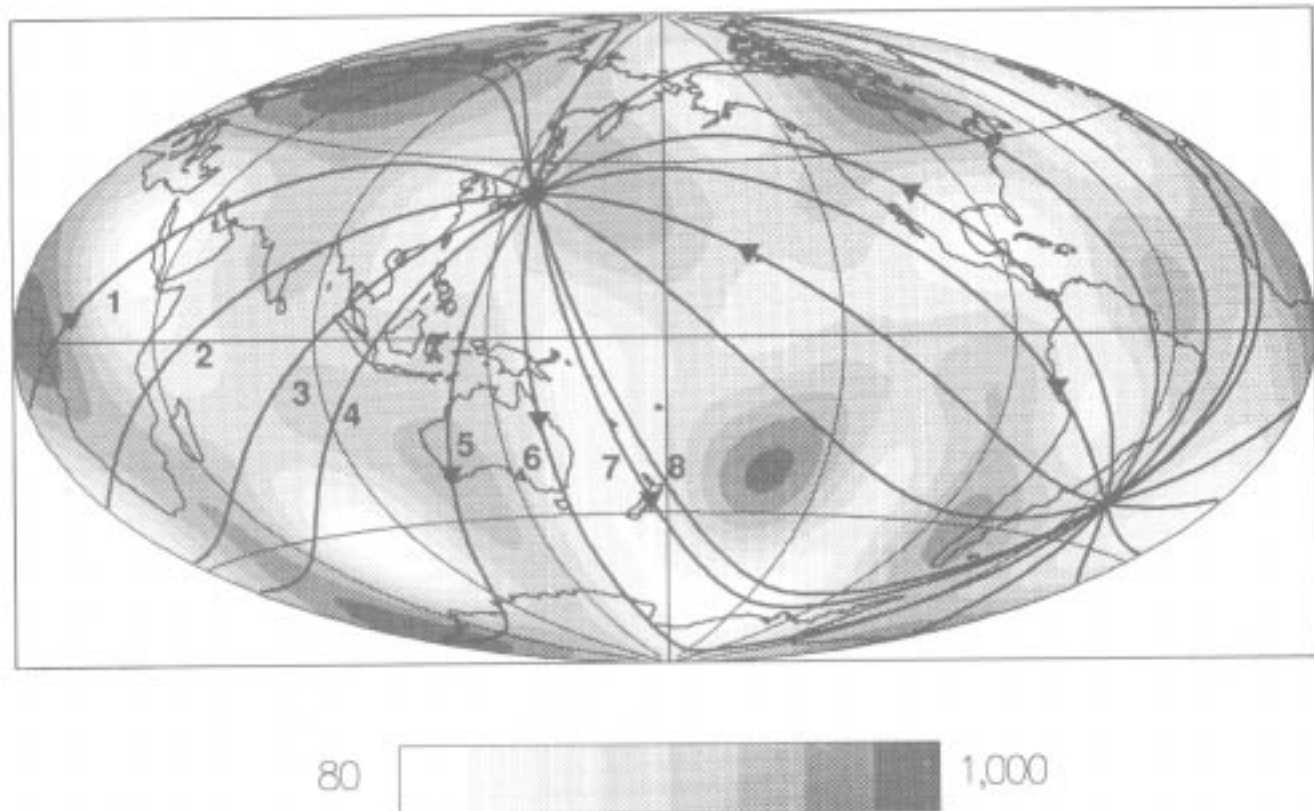
80   1,000

Figure 8. Eight source–receiver paths of varying path-averaged Q perturbation, $\delta\hat{Q}$, for the Japanese event of 1982 July 23. Stations selected are: (1) BCAO, (2) KIP, (3) NNA, (4) ANMO, (5) NWAO, (6) CTAO, (7) SNZO and (8) GRFO. The path of highest $\delta\hat{Q}$ is (5), which passes through the Canadian shield and the high Q anomaly off the Antarctic coast. The path of lowest Q is (4), which samples the low Q features of Central and South America. Also of note are paths (6), (7) and (8), which are all tangent to the low Q structures in the South Pacific, and thus have high average gradients transverse to the great circles.

in $(1/l)$, by

$$\delta\alpha_k = \delta\hat{\alpha}_k + \frac{\hat{d}_k}{2k}\tan\lambda_k.$$ (13)

This corresponds to equation (11) for elastic phase perturbations. $\delta\hat{\alpha}_k$ and $\hat{d}_k$ are path integrals of the imaginary parts of the complex structure terms

$$\delta\sigma_k = \delta\omega_k + i\delta\alpha_k$$ (14)

$$\mathscr{D}_k = D_k + id_k.$$ (15)

Finally, the phase shift brought about by anelastic perturbations may be approximated by

$$\psi_k^{anel} = \frac{a\Delta}{U}\left(-\overline{\delta\alpha}_k\tan\lambda_k + \frac{\hat{d}_k}{2k} + \frac{\cot\Delta}{8k}\overline{\delta\alpha}_k\sec^2\lambda_k\right).$$ (16)

The overbars here have the same meaning as in eq. (12).

For anelasticity, zeroth- and first-order phase shifts result solely from multiplet–multiplet coupling, and the amplitude signal is a self-coupling effect. The zeroth-order anelastic amplitude effect is the smooth trend in l given by eq. (9), which is derived from the first term in eq. (13). The first-order correction to this asymptotic prediction is an oscillating function of l due to gradients. This function has the same period as the oscillating parts of the elastic frequency and amplitude shifts (eqs 11 and 12). Higher

order asymptotic effects are expected to be less significant for the anelastic case than for the signal of elastic asphericity, because anelastic structure is relatively small, but non-asymptotic effects may still be significant for synthetics that violate the short-time approximation.

The equations for a non-isotropic source are not discussed here, but may be shown to have the same essential characteristics, as indicated by Romanowicz (1987).

3.3.2 Qualitative analysis

Observations of the elastic phase shift are familiar from such studies as Davis & Henson (1986), Romanowicz & Roult (1986) and Romanowicz (1987). Our observations of these effects in coupled normal mode synthetics closely resemble the data described and discussed by those authors. We need only emphasize that the phase signal of elastic self-coupling dominates the phase spectra, as illustrated in Fig. 3(b).

The functions $T_{self\rightarrow a,s}^{NM}$, exemplified by Fig. 7(a), characterize our synthetic observations of the normal mode amplitude signal due to elastic coupling of multiplets. These functions clearly display strong oscillations at the expected periods. The amplitudes of the oscillations are seen to be, in general, considerably larger than the magnitude of anelastic amplitude effects measured by $T_{c\rightarrow a}^{NM}$.

The periodic perturbation caused by cross-coupling is not

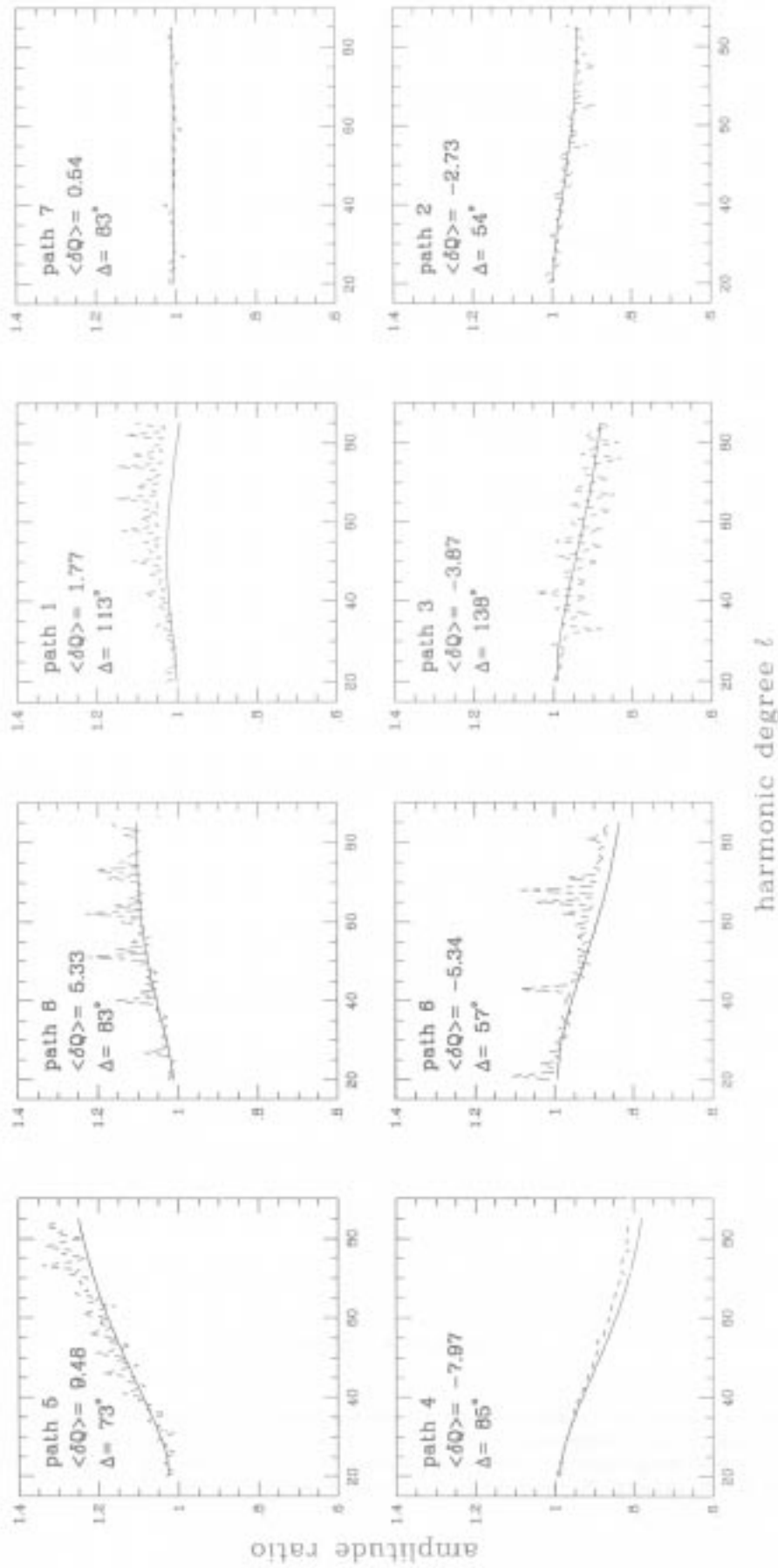**Figure 9.** Plots of $T_{\text{ratio}}^{\text{mod}}(l)$ for the coupled mode synthetic data and zeroth-order asymptotic theory, as in Fig. 7, for the paths of Fig. 8. Path labels are those of Fig. 8, and the values of $\langle \delta Q \rangle = \delta \bar{Q}$ are for $l = 30$.
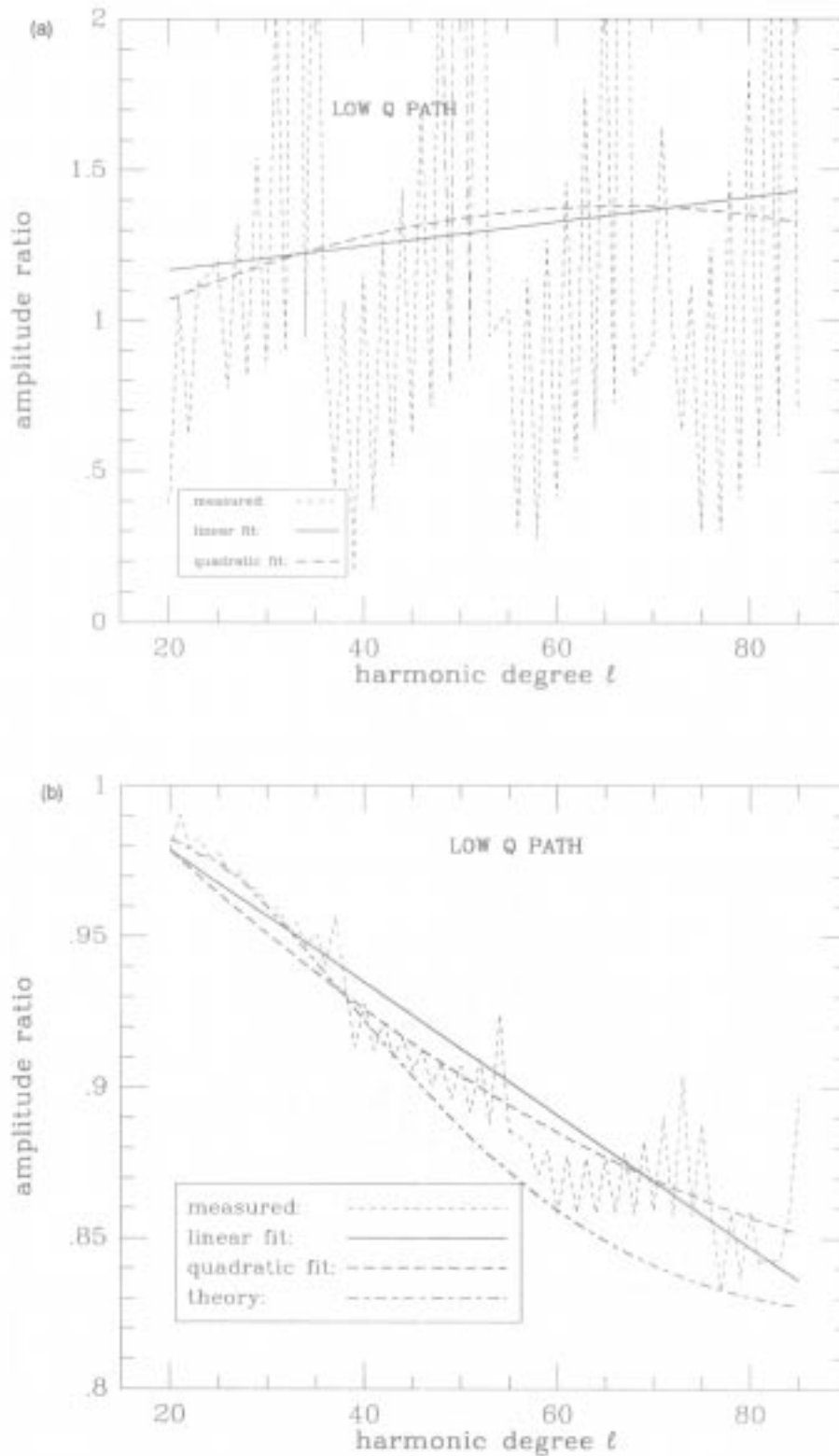
Figure 10. Examples of smooth *l*-polynomial fits to transfer functions. (a) The best fitting linear and quadratic polynomials to $T^{NM}_{R15 \to 415}(l)$ for the low Q path. Note that this transfer function closely resembles that of Fig. 7(a) and that the best fits are not similar to those for the anelastic transfer function below. (b) The best fitting linear and quadratic polynomials to $T^{bin}_{4 \to 4}(l)$ for the low Q path. The theoretical lines for zeroth-order asymptotic theory are also included. The linear and quadratic trends fit the data similarly.

the only significant part of the elastic amplitude signal. Fitting a linear or quadratic polynomial in l to the transfer functions for this signal,

$$T_{RH \to e}^{NM}(l) = A_e^{(\pm 5)}(l)/A_{RH}(l), \tag{17}$$

often reveals a smooth function of l, as seen in by Fig. 10(a). As demonstrated by Fig. 10, the amplitude perturbations represented by such smooth trends usually have magnitudes of the same order as the expected signal of anelastic structure. Such fits are not highly robust, implying that the removal of the periodic signal, a discretely undersampled tangent function, is non-trivial. The offsets are persistent, however, suggesting that they result from either the slowly varying first-order gradient term of eq. (12), higher order asymptotic effects, or non-asymptotic behaviour. Because significant smooth trends are observed for paths with small $\delta\bar{\omega}$, it is reasonable to attribute them primarily to the first-order gradient effect.

Our observations of $T_{e \to a}^{NM}$, exemplified by Figs 7(b) and 9, show that these transfer functions do, for the most part, take the form of the zeroth-order asymptotic trend, perturbed by an oscillating term. The oscillations dominate the signal for paths with small average Q perturbation, $\delta\hat{Q}$. It is also evident that, although the observed transfer functions are well fit by simple curves, the theoretical smooth transfer function does not fit the measured trend optimally. This is better illustrated in Fig. 10(b). Since such discrepancy is most often observed for paths of highest or lowest $\delta\hat{Q}$, it is probable that these observations are accounted for by violation of the short-time approximation.

Finally, Figs 7(b) and 9 do not show points corresponding to nodes in the RH model spectra. As explained in Appendix A, at such nodes eq. (13) is replaced by

$$\delta\alpha_k = \left(\frac{\hat{d}_k}{2k} - \frac{\cot \Delta}{8k} \delta\hat{\alpha}\right) \tan \lambda_k. \tag{18}$$

This expression lacks the smooth $\delta\hat{\alpha}$ term and produces a separate trend of ratio points centred on $A_k^{(anel)}/A_k^{(elas)} = 1$.

3.3.3 Statistical analysis

We use variance reduction statistics to quantify the success of asymptotic theory in predicting $T_{e \to a}^{NM}$. The variance reductions displayed in Table 2 are given by

$$\frac{\delta V}{V} = 1 - \frac{\sum\limits_{i,l} (\beta_{il}^{data} - \beta_{il}^{theory})^2}{\sum\limits_{i,l} (\beta_{il}^{data})^2}, \tag{19}$$

where β_{il} is $T_{e \to a}^{NM}(l)$ for path i. The data functions are either ratios of the measured synthetic peak amplitudes, or mathematically smoothed representations of the measured functions. The theoretical functions are given by eqs (A23) and (A27).

Simply subtracting the theoretical functions from the data reduces the variance of amplitude ratios by 55 per cent. Because the majority of our paths have small average Q anomalies, in which case the oscillating first-order term of eq. (13) dominates, this number is not the most relevant measure of how accurately the zeroth-order theory forecasts trends in the synthetic data. To provide a more informative evaluation of the theory, we must extract smooth trends

Table 2. Variance reductions produced by removing the anelastic amplitude effect forecast by asymptotic theory from the measured amplitude perturbations in synthetic normal mode multiplets, and from polynomial best fits to the measurements. The transfer function $T_{e \to a}^{NM}$, plotted as a function of harmonic degree l, isolates the effect of the anelastic component of the model. The theoretical trends are given by eq. (A28) and can be seen, in the case of isolated anelastic signal, to account for much of the observed variance, especially for the smoothed trends.

data	$T_{e \to a}^{NM}$ variance reduction
measured	55%
best linear fit	88%
best quadratic fit	86%

from the data. This is accomplished by fitting simple polynomials to the measured transfer functions. The zeroth-order asymptotics reduce the variance of best linear fits by 88 per cent. For quadratic fits the result is a virtually identical 86 per cent. Though polynomial fits are almost certainly not the best smoothing routines for these data, these variance reductions indicate that the zeroth-order asymptotic theory predicts the smooth component of the measured transfer functions quite well.

Similar variance analysis also indicates that it is virtually impossible to identify either real or theoretical $T_{e \to a}^{NM}$ in the overall amplitude signal from aspherical structure. One per cent or less of the variance of the smoothed transfer functions

$$T_{RH \to a}^{NM}(l) = A_{anel}^{(\pm 5)}(l)/A_{RH}(l) \tag{20}$$

is reduced by removing $T_{e \to a}^{NM}$. Apparently, the smooth trends in amplitude anomalies due to elastic structure, together with the difficulty in robustly fitting the strong periodic component of $T_{RH \to e}^{NM}$, completely obscure the anelastic transfer functions.

3.3.4 Summary and implications

These observations and statistics are evidence that separating the signals of elastic and anelastic asphericity in normal mode spectrum is not trivial, and, in particular, is not accomplished simply by removal of the tan λ_k pattern in the perturbed amplitudes. The zeroth-order periodic component of $T_{self \to \pm 5}^{NM}$ directly masks the first-order part of the anelastic signal, which has the same period. In addition, the strong oscillations of $T_{self \to \pm 5}^{NM}$ are difficult to eliminate in a robust manner, especially for a narrow spectral range.

Even after smoothing the periodic component of $T_{RH \to a}^{NM}$, it is likely that a significant part of the remaining signal is contributed by elastic structure, through first- and higher order cross-coupling effects forecast by asymptotic theory, as well as non-asymptotic effects. This elastic signal appears to be strong enough to interfere with the zeroth-order anelastic transfer functions, which would, if measurable, provide a simple data set from which to estimate

long-wavelength aspherical Q. Because of the ambiguity in the source of amplitude anomalies, phase data, (which, as illustrated by Fig. 3(b), are virtually uncorrupted by an anelastic signal for the wavelengths considered here) must be incorporated in order to separate the effects of elastic and anelastic structure in the data. This may be accomplished by employing an *a priori* elastic model constructed using phase data, as did Durek *et al.* (1993), or by performing joint elastic–anelastic inversions using both phase and amplitude data. At present, no joint inversions have been performed, but a number of aspherical elastic models constructed using long-period phase data exist, including those of Masters *et al.* (1982), Nakanishi & Anderson (1982, 1983, 1984), Nataf, Nakanishi & Anderson (1984, 1986), Tanimoto & Anderson (1984, 1985), Davis (1987), Smith & Masters (1989), Montagner & Tanimoto (1991), Masters, Bolton & Shearer (1992) and Su, Woodhouse & Dziewonski; (1993).

Variance reductions of over 85 per cent for best fitting polynomials to measured $T^{NM}_{e \to a}$ transfer functions imply that zeroth-order asymptotic theory provides a good description of the amplitude effects of long-wavelength anelastic structure, over and above those of elastic structure. Therefore, when aspherical elastic structure and the resulting amplitude signal are known, an appropriately smoothed $T^{NM}_{e \to a}$, interpreted with asymptotic theory, should prove useful for modelling aspherical Q from normal mode measurements.

4 RAYLEIGH WAVEPACKET AMPLITUDE PERTURBATIONS

4.1 Measurements

Measurements of surface wave amplitudes are performed on Rayleigh wavepackets excised from the synthetic seismograms. To measure the waveform parameters at the centre frequency of a given multiplet, we first calculate the expected group arrival times of that frequency component of R_1 through R_8 using the group velocity of the spherical earth multiplet. For each arrival time, t_n, a half-hour segment centred on t_n is excised from the synthetic time series and the Fourier transform of that segment is used to find the amplitude of the specified component frequency for that wavepacket, as illustrated in Fig. 11. For each modal frequency in the chosen range, we record two sets of amplitude ratios, which characterize the effects of elastic and anelastic structure together and anelastic structure alone, for wavepackets R_1 through R_8. These may be expressed, respectively, as

$$T^{SW}_{RH \to a}(n) = A^{(\pm 5)}_{anel}(n)/A_{RH}(n), \tag{21}$$

and

$$T^{SW}_{e \to a}(n) = A^{(\pm 5)}_{anel}(n)/A^{(\pm 5)}_{elas}(n), \tag{22}$$

where SW indicates that these are surface wave transfer functions, which are plotted as functions of orbit index n.

4.2 Observations

As in our investigation of modal spectra, we examine first the average amplitude perturbations for the set of 331 source–receiver paths. Results analogous to Fig. 3 are shown in Fig. 12, where we have plotted the trends for each wavepacket separately. Fig. 12(a) shows the averages of the magnitudes of the total amplitude perturbations due to both elastic and anelastic aspherical structure relative to RH amplitudes. The size of the amplitude signal is roughly proportional to both harmonic degree and wavepacket index, and for the highest frequency multiplets in this study, RH earth amplitudes are perturbed by aspherical elastic and anelastic structure anywhere from a modest 10 per cent for R_1, to 28 per cent for R_4, to approximately 44 per cent for the case of the R_8 wavepackets.

The part of this amplitude effect attributable to the introduction of long-wavelength anelasticity is displayed in Fig. 12(b) as the averages of the absolute values of the anelastic ± 5 to elastic ± 5 amplitude ratios. At $l = 85$, aspherical anelasticity perturbs the amplitudes of the elastic ± 5 synthetics by 2, 15 and 28 per cent for R_1, R_4 and R_8, respectively. It is also evident that not only does the average magnitude of the anelastic amplitude signal increase with wavepacket index and harmonic degree, but so too does the size of the perturbation due to anelasticity as a fraction of the total amplitude signal shown in Fig. 12(a). At $l = 85$, and for higher orbits, the anelastic contribution is about half of the total perturbation in surface wave amplitudes. This is a stronger effect than is seen in the amplitudes of normal mode spectra, where, for the multiplets measured, the anelastic asphericity accounts for at most about a third of the total perturbation in amplitudes (Fig. 3). This observation reflects the fact that the 15 hr time series we transform to produce the normal mode spectra are dominated by the first few surface wavepackets, which in Fig. 12(b) show smaller anelastic amplitude perturbations than the later Rayleigh wave arrivals.

We have also measured surface wave phase perturbations, but the phase perturbations attributable to aspherical attenuation were found, on average, to be negligibly small compared with the effects of elastic structure and normal noise levels, and the details of these measurements are not presented.

Figure 13 displays amplitude measurements for the high and low Q paths (Fig. 4) at a frequency of 5.611 mHz, which corresponds to the $l = 50$ multiplet. We plot $\ln(T^{SW}_{RH \to a})$ as a function of wavepacket index, and, for comparison, we also display the natural logarithm of the elastic transfer function

$$T^{SW}_{RH \to e}(n) = A^{(\pm 5)}_{elas}(n)/A_{RH}(n). \tag{23}$$

For the elastic amplitude anomalies, each path shows a distinct pair of trends, one for even and one for odd index orbits. The pattern does not, however, display the symmetry of opposite slopes anticipated by linearized ray theory, and is similar to the results displayed by Woodhouse & Wong (1986) and Durek *et al.* (1993). Introducing the long-wavelength anelastic model appears to rotate the pattern for each path; downward for the low Q path and upward for the high Q path. Closer inspection reveals that the slopes of the even and odd trends in each case are approximately shifted by a constant.

Alternatively, the nature of the effects of the aspherical anelastic model on the amplitudes of Rayleigh wavepackets can be illustrated by plotting $\ln(T^{SW}_{e \to a})$ against wavepacket index. Such transfer functions for the high and low Q paths
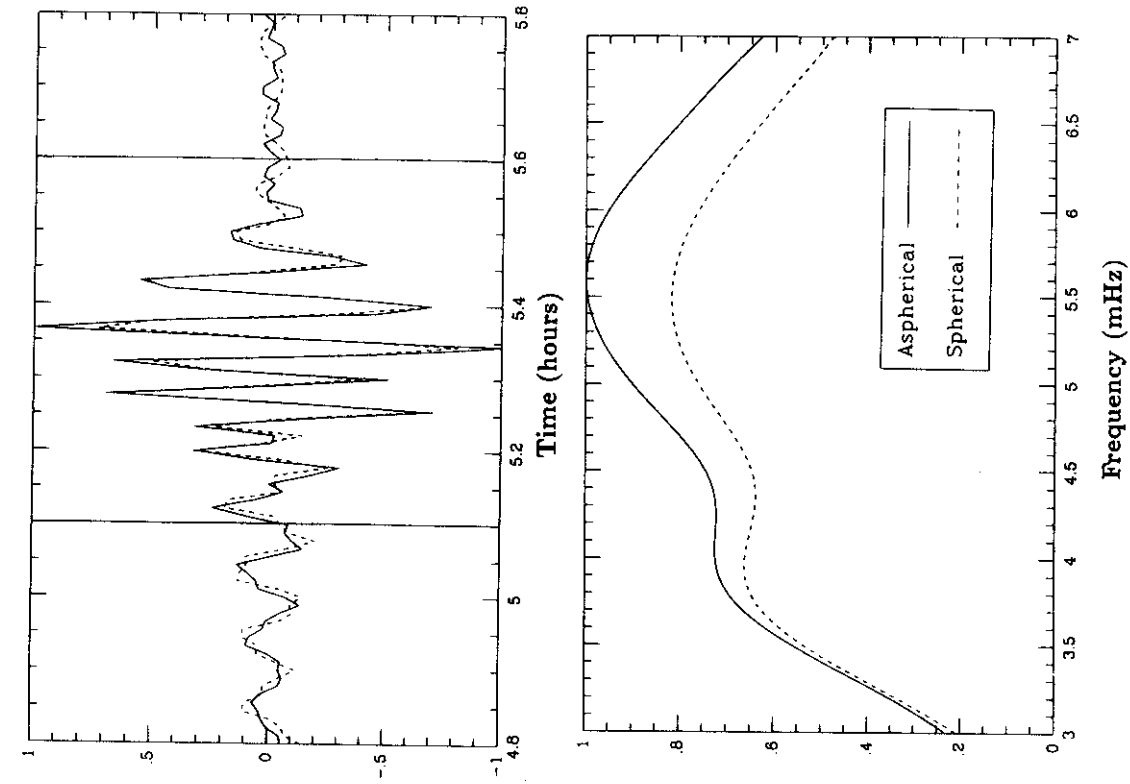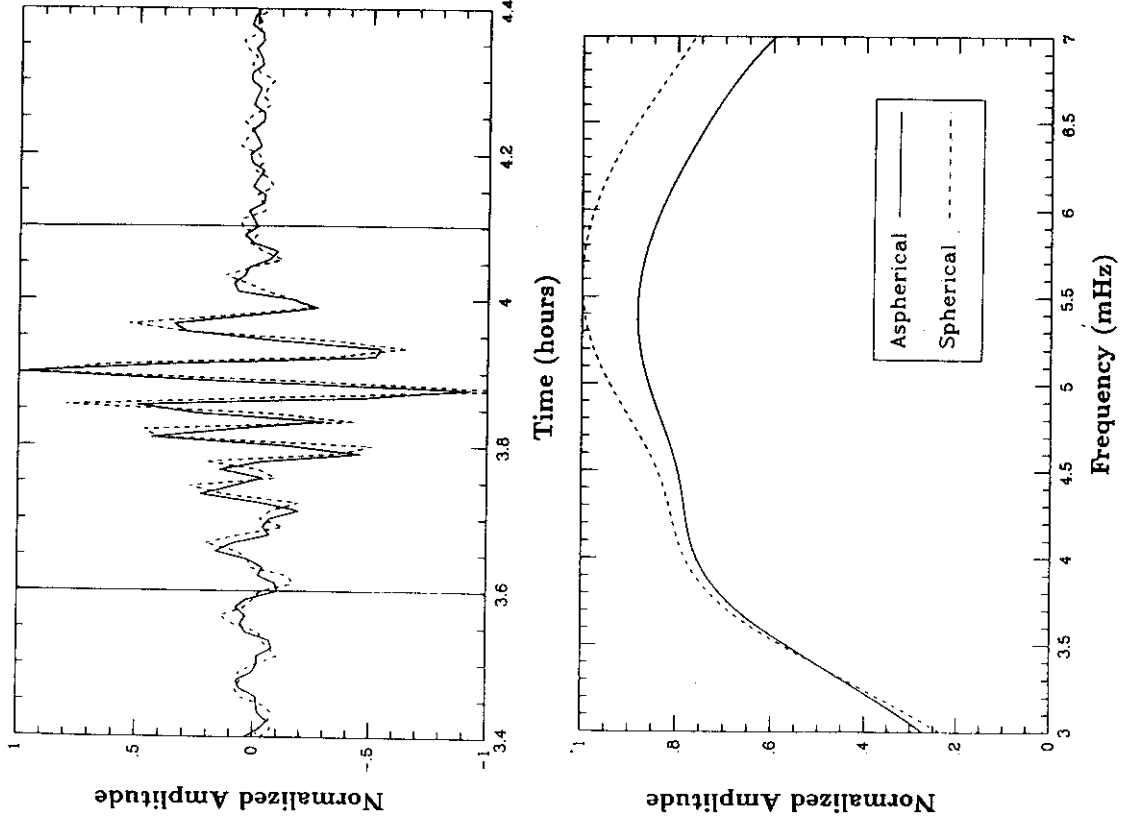
Figure 11. Illustration of wavepacket excision. The upper plots show unit normalized portions of the synthetic time series constructed for the high and low Q paths of Fig. 4. The Rayleigh wavepackets shown are R_3 and R_4, as indicated. Spherical and anelastic ±5 (aspherical) synthetics are displayed as dashed and solid lines, respectively. The vertical lines in the upper plots are the boundaries of the time windows used for the Fourier transforms. The normalized spectra that result from the transforms are displayed in the lower plots. In both the time and frequency domains, it can be seen that, as anticipated, low Q paths display lowered amplitude while high Q paths display increased amplitude.
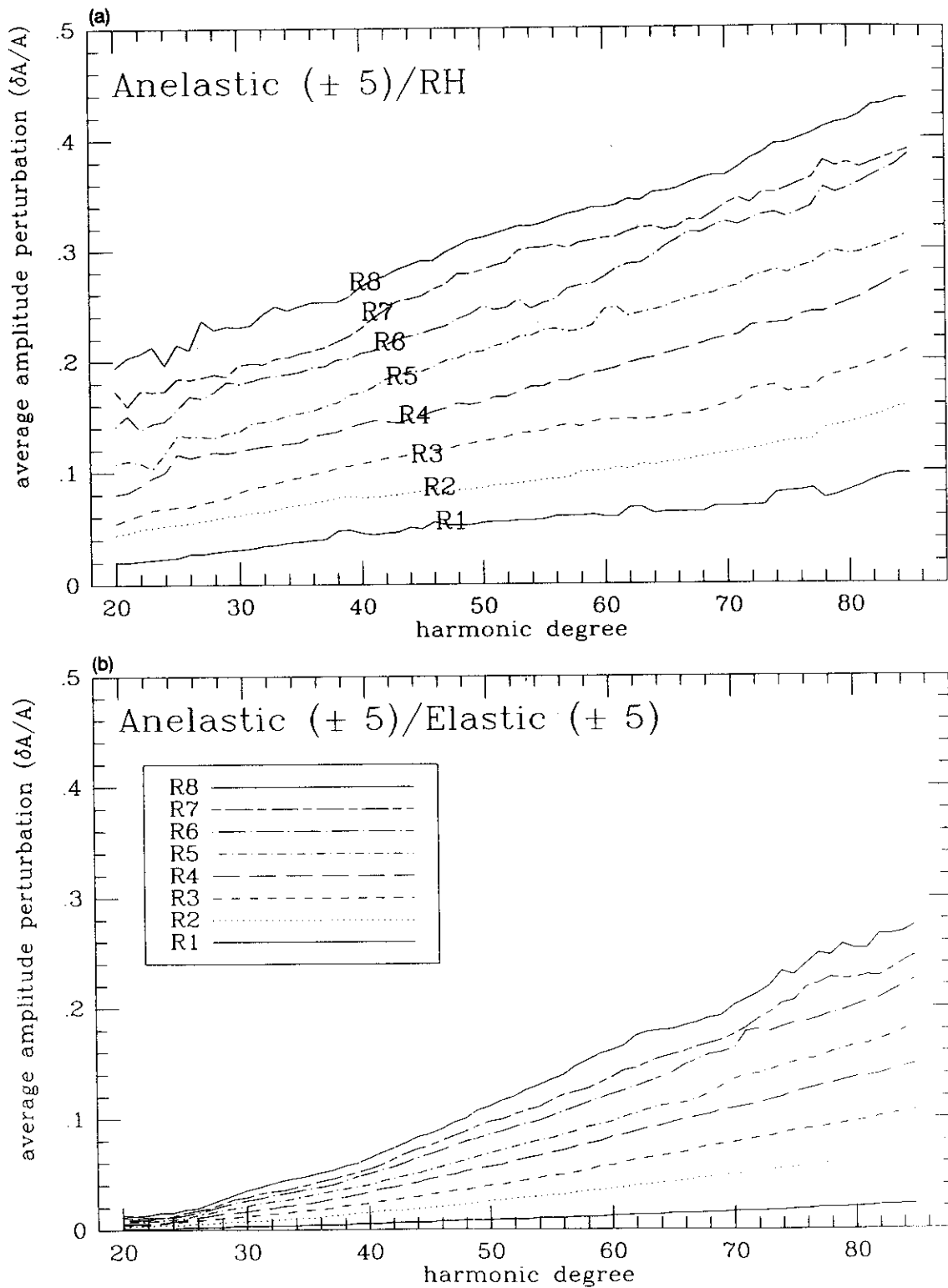
Figure 12. Perturbations in wavepacket amplitude as a function of harmonic degree for Rayleigh wavepackets R_1-R_8. A separate trend is plotted for each wavepacket index. Each point represents an average, over 331 synthetics, of the magnitude of the perturbations $(\delta A/A) = 1 - (A'/A)$. A and A' are amplitudes at the specified frequency obtained from the spectrum of the excised wavepackets of a 'reference' and a 'perturbed' synthetic. In (a), the reference synthetics are RH and the perturbed synthetics are anelastic ±5, so that the amplitude perturbations shown are the result of general elastic and anelastic aspherical structure. In (b), the reference becomes the elastic ±5 synthetics, so that (b) represents the contributions to the perturbations in (a) from anelastic asphericity alone.
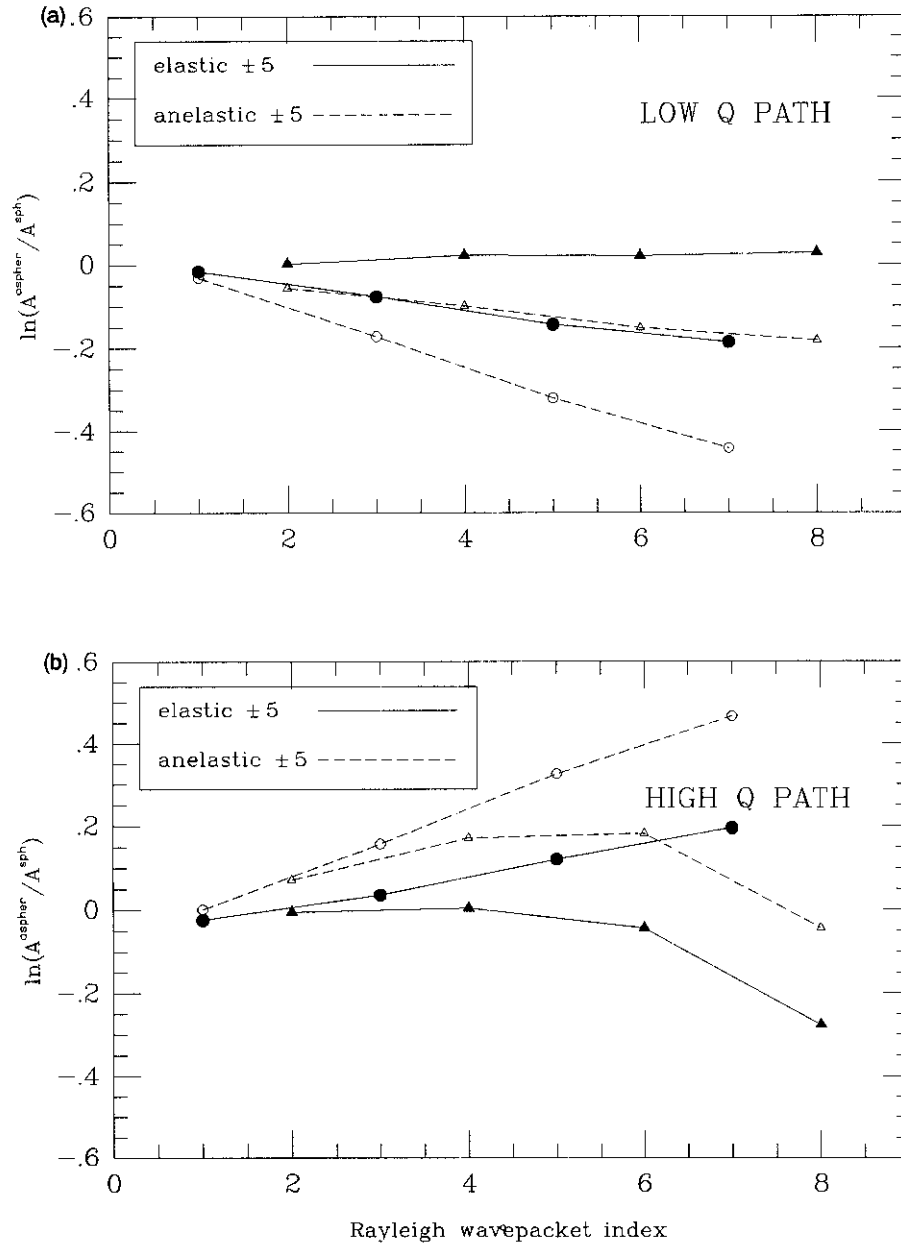
Figure 13. Surface wave amplitude perturbations ln $(T^{SW}_{RH \to e})$ and ln $(T^{SW}_{RH \to a})$, at $l = 50$, plotted as a function of wavepacket index for the high and low Q paths. Separate trends are plotted for odd (circles) and even (triangles) index wavepackets. The effect of the anelastic asphericities is roughly to rotate the pattern of perturbations that results from elastic asphericities; upward for the high Q path and downward for the low Q path.

at 5.611 mHz are shown in Fig. 14. It is clear that in each case the perturbations for odd- and even-order wavepackets approximate a single linear trend, as one would expect if the paired slopes of Fig. 13 are shifted by the same constant. Also shown in this figure are theoretical lines with slope

$$\gamma'_k = \frac{\pi \omega_k a}{2 u_k Q_k} \left(\frac{\delta \hat{Q}_k}{Q_k} \right), \tag{24}$$

where a is the radius of the earth and u_k is the group velocity of the unperturbed multiplet. This prediction is derived from linearized ray theory and is discussed in greater detail in the next section and in Appendix B.

That the transfer functions ln $(T^{SW}_{e \to a})$ tend to curve as

wavepacket index increases is evident in Fig. 14. Such deviations from linearity become much more pronounced at higher frequencies. Fig. 15 illustrates this by showing the high and low Q path transfer functions at a series of multiplet indices corresponding to increasing frequencies. As frequency is increased, the magnitude of transfer function slopes also increases. At the same time, the even- and odd-order trends tend to separate and become less linear for the later arriving wavepackets. Fig. 16, which shows the $l = 50$ transfer functions for the set of eight paths of Fig. 8, demonstrates that while the general slope of the transfer function is correlated with the average Q anomaly, $\delta \hat{Q}_k$, of a path and with the expectations of linearized ray
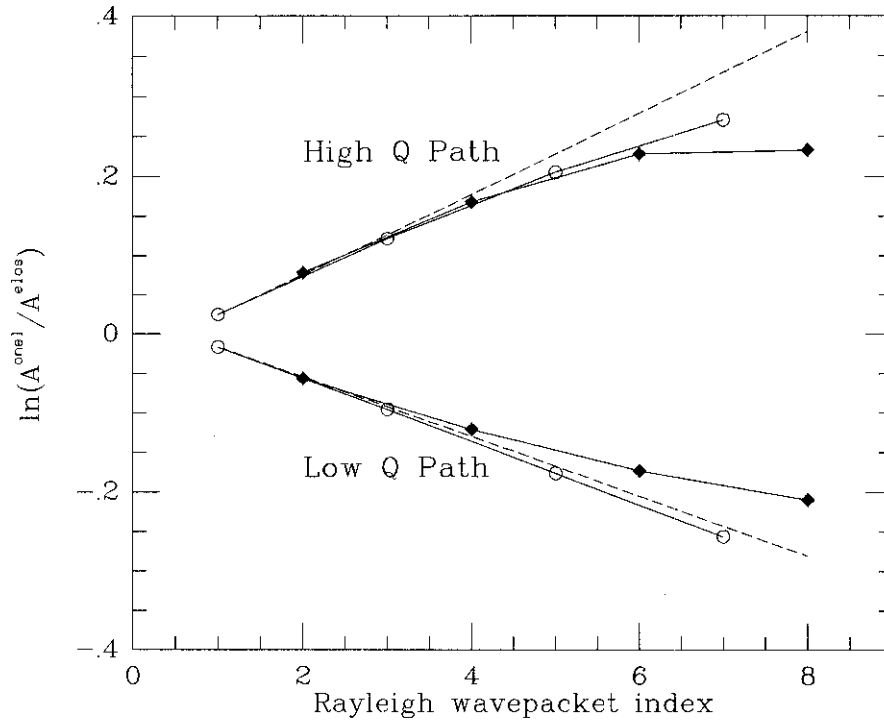
Figure 14. ln $(T_{c \to a}^{SW})$ at $l = 50$ for the high and low Q paths. Plotted as dotted lines are the theoretical slopes, γ', predicted by linearized ray theory and given by eq. (24).

theory, the size and nature of deviations from linearity can vary greatly from path to path.

The observed deviations are strongest for paths across which there are relatively large gradients of aspherical structure. In Fig. 15, the transfer functions of the high Q path show much greater separation and non-linearity than do those of the low Q path. Referring back to Fig. 4, we see that the high Q path lies tangent to structural contours through much of its length in Asia and Northwest Africa and, thus, is a high gradient path compared with the low Q path which is tangent to contours only briefly in the South Pacific. In Fig. 8, we can see that paths 6, 7 and 8 all pass through the steep gradients on the sides of the extended low Q 'valley' in the South Pacific, but have three different orientations with respect to that feature. In Fig. 16 these three paths display three different types of strong non-linear deviation.

4.3 Discussion

4.3.1 Theoretical expectations

The linearized ray theory (LRT) developed by Woodhouse & Wong (1986), and generalized by Romanowicz (1990) and Durek *et al.* (1993) to account for aspherical anelasticity, is summarized briefly in Appendix B. This theory has two important predictions relevant to our observations. First, in the case of an elastic earth model, aspherical structure focuses or defocuses surface waves depending on the direction of travel between source and receiver. As a consequence, the theory predicts that the amplitude ratio $r_k(n) = [A_k^{(\text{elas})}/A_k^{(\text{RH})}]$, plotted on a logarithmic scale as a function of Rayleigh wavepacket index n, will produce two

straight lines of opposite slopes, for arrivals of odd and even index. This implies

$$\frac{\ln [r_k(n + 2)] - \ln [r_k(n)]}{2}$$

$$= \frac{\ln [r_k(n + 1)] - \ln [r_k(n + 3)]}{2}, \qquad (25)$$

or

$$d_{kn} \equiv \frac{r_k(n + 2)r_k(n + 3)}{r_k(n)r_k(n + 1)} = 1. \qquad (26)$$

Second, surface wavepackets on an earth model with aspherical attenuative structure, travelling on a great circle with average Q perturbation $\delta \bar{Q}$, accumulate an amplitude perturbation which adds to the slope of each of the elastic trends the value γ_k' as defined in eq. (24). γ_k' is the net slope for even and odd wavepackets combined, so that

$$\frac{\ln [r_k(n + 2)] - \ln (r_k(n))]}{2} - \gamma_k'$$

$$= \gamma_k' + \frac{\ln [r_k(n + 1)] - \ln [r_k(n + 3)]}{2}, \qquad (27)$$

and

$$d_{kn} = \exp (4\gamma_k'). \qquad (28)$$

In addition, we anticipate that lateral gradients in earth structure cause the surface waves to deviate from the great circle paths used to calculate the linearized elastic and anelastic amplitude effect, leading to the failure of LRT for multiply orbiting waves. Path deviations accumulate with each circuit of the Earth, so that the magnitude of
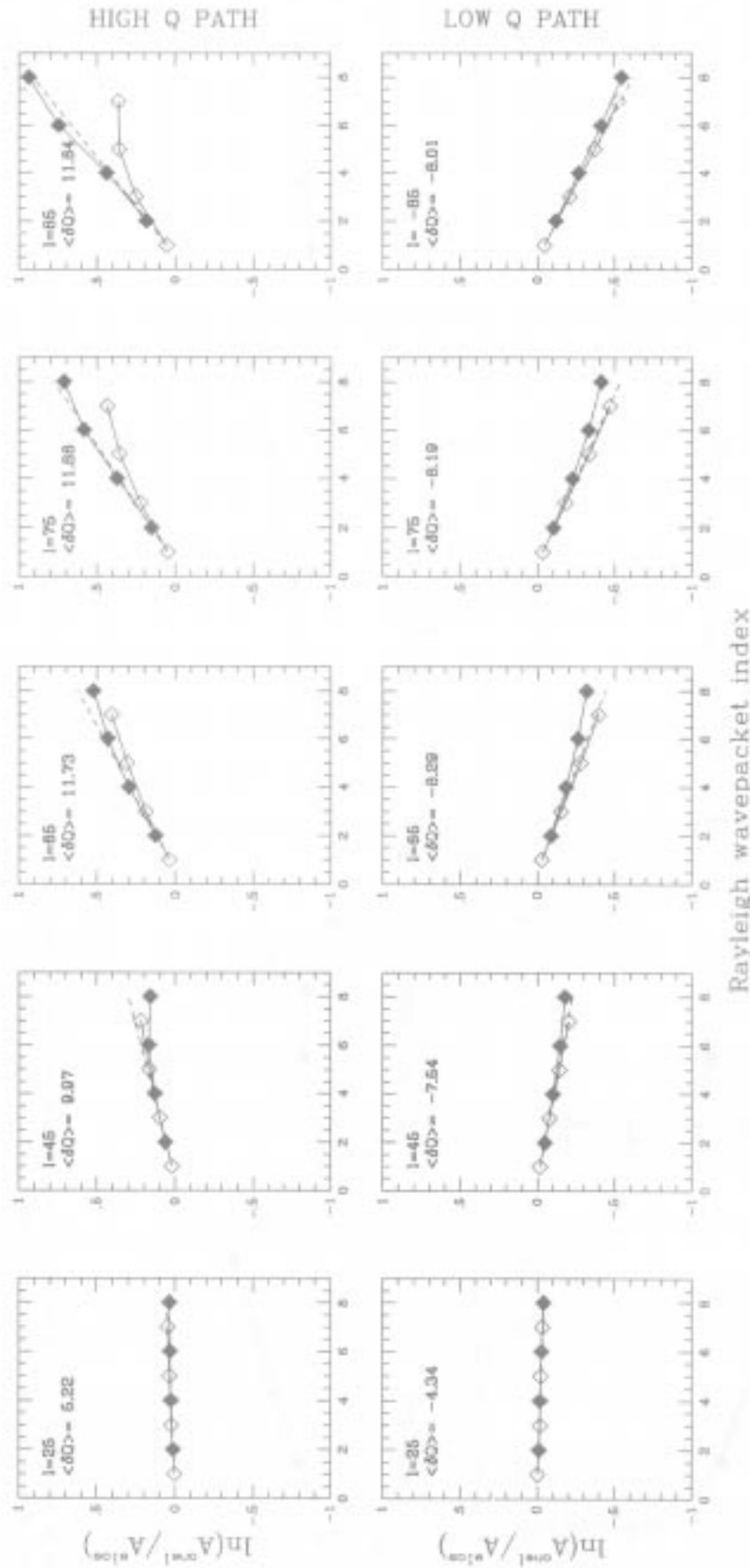
Figure 15. Sequences of surface wave transfer functions ln $(T_{r=a}^{SW})$ superimposed on theoretical lines as in Fig. 14. The results for harmonic degrees $l = 25, 45, 65, 75, 85$ are shown for the sample high and low Q paths. The corresponding values of the path-averaged aspherical Q perturbation, $\langle \delta Q \rangle = \delta \bar{Q}_{a(l)}$, are also indicated. The non-linear effects of path wander are stronger for higher harmonic degrees.

Figure 16. ln (T^{sw}_{n-n}), plotted as in Fig. 14, for the paths shown in Fig. 8. Positive correlations of the slopes of the transfer functions and path-averaged aspherical Q perturbation, $\langle \delta Q \rangle$, is evident, as are strong non-linear trends for several paths, attributable to path wander.

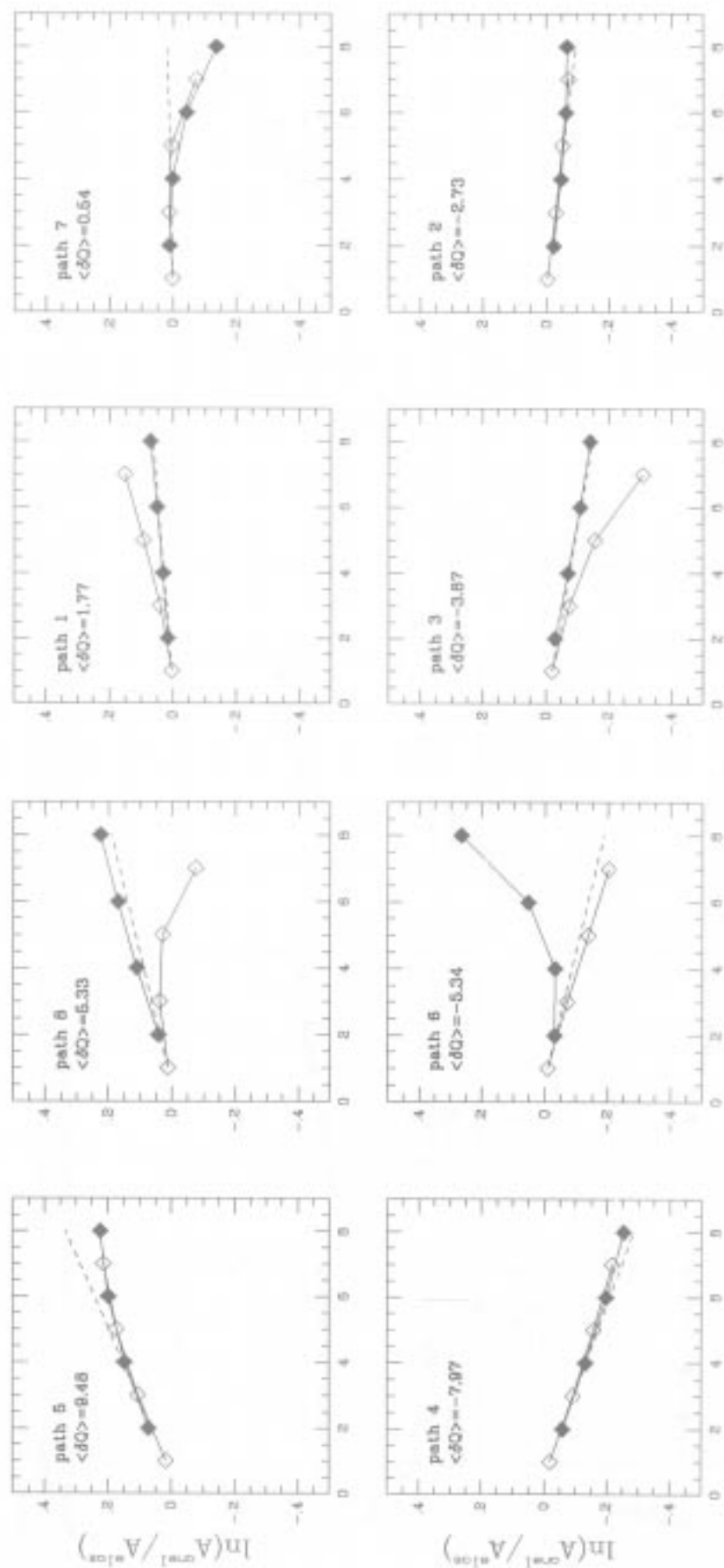departures from the predictions of LRT is expected to increase with wavepacket index. Wavepackets travelling in opposite directions will be bent differently, so that the LRT amplitude effect will be perturbed differently for odd and even index arrivals. In particular, the colinear trends LRT forecasts for the anelastic case will be separated by path wander. Also, the sign of the relevant gradient term is such that paths tend to wander away from high-velocity regions and into low-velocity zones, so that, as noted by Woodhouse & Wong (1986), multiply orbiting surface waves can become trapped in low-velocity paths. The proportionality of velocity and Q (eq. 6) thus implies that path-averaged Q will be, on average, lowered for multiply orbiting surface waves, resulting in the depression of average amplitudes.

4.3.2 Qualitative analysis

Our synthetic observations of amplitude perturbations produced by elastic structure, like those of Woodhouse & Wong (1986), most often show only rough agreement with the first-order predictions of LRT. Fig. 13 gives two examples of synthetics that display trends which are separate for even and odd orbits, but neither reciprocal nor even linear. Such discrepancy is clearly inherited by the overall signal of elastic and anelastic structure.

The part of the amplitude signal due solely to aspherical anelastic structure appears much better forecast by LRT. The observed trends displayed in Figs 14 and 15, in contrast with the elastic signal of the Fig. 13, nearly overlie the theoretical values. This is true even for the high Q path, which may be seen in Fig. 4 to be characterized by the strong gradients expected to produce path wander. Only for frequencies of 8 mHz or more, which are more sensitive to the shorter wavelength structures in our model, do the observations for that path exhibit significant non-linearity (Fig. 15). Good agreement between anelastic LRT and coupled synthetic data is generally observed, although the paths of some synthetics, including paths 6 and 8, do sample structures in such a way as to produce larger deviations.

The deviations from LRT are seen to exhibit several of the identifying characteristics of path wander. Anomalies are usually larger for paths that sample high-gradient regions. In Figs 14–16 the anomalies are seen to distinguish odd and even trends and to increase with wavepacket index, as anticipated. Evidence for attraction to slow, low Q, paths is also observed. Amplitudes are, on average, depressed, though small or intermediate Q anomalies, together with strong gradients of structure near source or receiver, can produce exceptions such as those observed for paths 1 and 7.

4.3.3 Statistical analysis

Table 3 quantifies the extent to which LRT succeeds in forecasting elastic amplitude anomalies by displaying $\|d_{kn} - 1\|$, the rms average deviation from unity of d_{kn}, for an array of different modal and wavepacket indices. Departures from LRT are seen to increase with n, from 0.11 to 0.21 as n varies from 1 to 5 at $l = 50$, and with l, more than doubling for $n = 1$ as l varies from 25 to 75. Path wander, which is stronger for surface waves with shorter wavelengths, and which accumulates with each orbit, can account for each of these trends.

If LRT were assumed to apply exactly for these synthetics, the values for $\|d_{kn} - 1\|$ in Table 3 would be misinterpreted as the result of anelastic structure, through eq. (28). We can use this expression and eq. (24) to solve for the aliased path-averaged Q perturbation, $\delta\hat{Q}_{\text{alias}}$, from elastic structure

$$\delta\hat{Q}_{\text{alias}} = \left(\frac{u_k Q_k^2}{2\pi a \omega_k}\right) \ln\,(d_{kn}) = g(k)\ln\,(d_{kn}). \tag{29}$$

The function $g(k)$, which is highest for the low-frequency multiplets with high modal Q, determines the sensitivity of the multiplets to elastic aliasing. Table 3 displays the values of $\delta\hat{Q}_{\text{alias}}$ calculated for each value of $\|d_{kn} - 1\|$ in that table. The numbers in Table 3 are better interpreted through comparison with the largest Q perturbations produced by the anelastic model at each frequency, $\delta\hat{Q}_{\text{max}}$,

Table 3. Effectiveness of data 'desensitizations' and estimates of the resulting aliased $\delta\hat{Q}$ from elastic amplitude perturbations. $d_n = (R_{n+2}R_{n+3})/(R_n R_{n+1})$ where n is the Rayleigh wavepacket index. Reported values are rms averages over all paths, winnowed at three standard deviations. Aliased $\delta\hat{Q}$ values at $l = 25,50,75$ are compared with $\delta\hat{Q}$ from anelastic structure on the high Q path, which represents the largest perturbation used in this study.

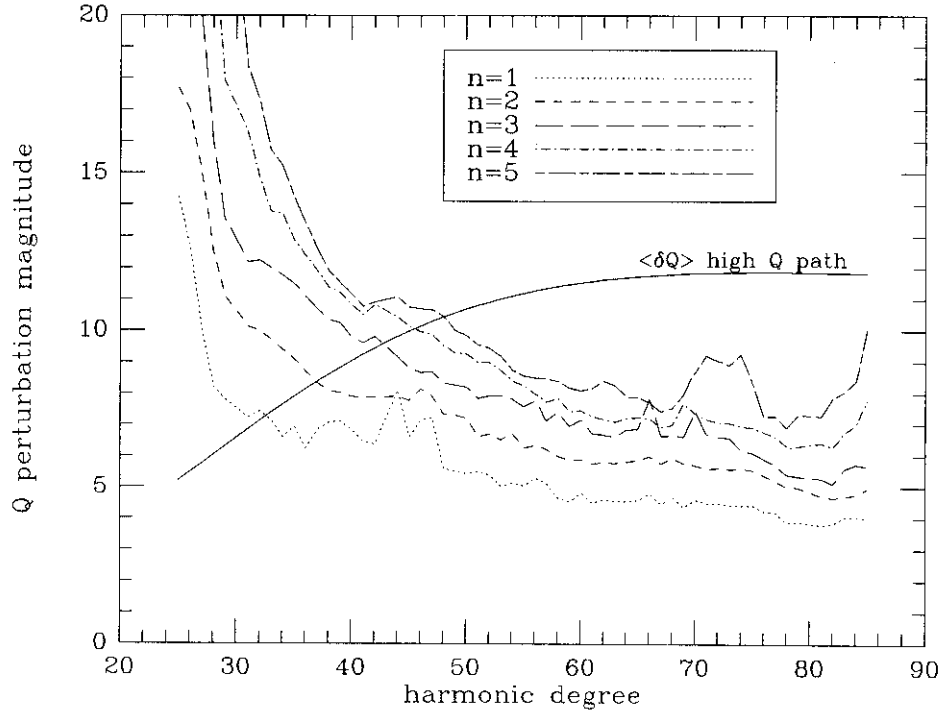|	$l = 25$			$l = 50$			$l = 75$		
n	$\|(d_n - 1)\|$	$\delta\hat{Q}_{\text{alias}}$	$\frac{\delta\hat{Q}_{\text{alias}}}{\delta\hat{Q}_{\text{max}}}$	$\|(d_n - 1)\|$	$\delta\hat{Q}_{\text{alias}}$	$\frac{\delta\hat{Q}_{\text{alias}}}{\delta\hat{Q}_{\text{max}}}$	$\|(d_n - 1)\|$	$\delta\hat{Q}_{\text{alias}}$	$\frac{\delta\hat{Q}_{\text{alias}}}{\delta\hat{Q}_{\text{max}}}$
1	.08	~ 15	280%	.11	~ 6	55%	.17	~ 5	40%
2	.10	~ 20	380%	.15	~ 8	75%	.22	~ 6	50%
3	.13	~ 25	480%	.17	~ 9	85%	.24	~ 7	60%
4	.18	~ 35	680%	.19	~ 10	95%	.27	~ 8	70%
5	.27	~ 50	960%	.21	~ 11	100%	.34	~ 10	85%

Figure 17. Aliased $\delta\hat{Q}$ from the amplitude effects of elastic structure, as functions of harmonic degree for wavepacket indices $n = 1$–5. Shown for comparison is the trend for $\delta\hat{Q}$ resulting from anelastic structure in the model for the high Q path. In general, elastic aliasing becomes less significant at higher frequencies.

which correspond to the perturbations for the high Q path. The $l = 25$ multiplet is relatively insensitive to structure in the upper mantle, where the anelastic structure of the model is located. The path-average Q perturbation is thus small for this multiplet, and since its Q is high, making it sensitive to aliasing, the relative aliasing produced for $l = 25$ is extremely high. Modal Q is lower and upper mantle sensitivity is higher for $l = 50$ and $l = 75$, but average aliasing is still near 50 per cent of the maximum amplitude effect from anelasticity, even for $n = 1$, where aliasing is weakest.

This point is further illustrated by Fig. 17, which displays the average aliasing for the 3–9 mHz frequency range. The function $g(k)$ declines quickly with frequency, and greatly magnifies the aliasing for only low l multiplets, which are not expected to obey LRT well. For mid-range frequencies, 4–6 mHz, aliased $\delta\hat{Q}$ for $n = 1$ or $n = 2$ is about half as large as that from realistic anelasticity along the high Q path. Further increasing the frequency slightly decreases the relative size of the aliasing, but the improvement is not dramatic, and at higher frequencies it is expected that the effects of shorter wavelength elastic structure, not included in our model, will become more significant. Because of the strength of aliasing observed, which is never weaker than the average aspherical Q signal throughout the frequency range considered, it is unreasonable to rely on LRT to remove the elastic signal from surface wave amplitude measurements.

LRT may still be applicable to the interpretation of $T_{e \to a}^{SW}$ functions, which can be retrieved from $T_{RH \to a}^{SW}$ by employing

an *a priori* elastic model. Table 4 summarizes the success of eq. (24) in explaining the variations in net slope of the transfer functions $T_{RH \to a}^{SW}(n)$ and $T_{e \to a}^{SW}(n)$. Because LRT predicts that the transfer functions will be linear, we find, for each measured transfer function the slope of the line that best fits the logarithmic trend, and we report variance reductions of the form

$$\frac{\delta V}{V} = 1 - \frac{\sum_i (\beta_i^{data} - \gamma_i')^2}{\sum_i (\beta_i^{data})^2}, \tag{30}$$

Table 4. Variance comparisons of the measured and predicted signals of aspherical anelastic structure in synthetic Rayleigh wavepacket amplitudes. The data slopes are best fits to the $\ln[T^{SW}(n)]$ transfer functions defined by eqs (21) and (22), for the first three or first eight Rayleigh wavepackets. The theoretical slopes are γ', from linearized ray theory, as defined in eq. (24). Recorded are the variance reductions accomplished by removing the theoretical slopes from each type of measured slope.

slopes compared		orbits	variance reduction		
data	theory		$l = 25$	$l = 50$	$l = 75$
$\ln(T_{e \to a}^{SW})$	γ_{LRT}'	$R_1 - R_3$	62%	67%	67%
		$R_1 - R_8$	43%	54%	48%
$\ln(T_{RH \to a}^{SW})$	γ_{LRT}'	$R_1 - R_3$	2%	18%	28%
		$R_1 - R_8$	3%	13%	28%

where β is best fit slope and 'data' are either $\ln(T_{RH\to a}^{SW})$ or $\ln(T_{e\to a}^{SW})$. Because we anticipate greater departures from LRT in later arriving wavepackets, we compile separate statistics for the best fits to the trends of R_1–R_3 and R_1–R_8.

Throughout the spectral range considered, LRT accounts for about 65 per cent of the variance in the slopes of the R_1–R_3 surface wave amplitude trends due to anelasticity alone. This is comparable with the success of asymptotic theory in predicting the simplest normal mode amplitude effect of anelastic structure. As the relative strengh of the anelastic amplitude signal increases with l (Fig. 12b), the fact that the linear transfer functions of LRT account for much of this signal implies that the ability of LRT to forecast the trends of the overall amplitude effect will improve. Indeed, while LRT accounts for less that 3 per cent of the variance of $\ln(T_{RH\to a}^{SW})$ at $l = 25$, it explains nearly 30 per cent of the variance at $l = 75$. As expected, LRT in general explains a smaller percentage of the trends when later wavepackets, subject to more path wander, are included.

4.3.4 Summary and implications

Surface wave amplitude measurements for elastic ±5 synthetics reveal significant departures from LRT that would severely bias inversions of data for anelastic structure, if LRT alone were used to model the effects of elastic structure. By illustrating the l-dependence of the aliasing of elastic amplitude effects, the results displayed in Table 4 and Fig. 17 complement those of Durek *et al.* (1993), who demonstrated the importance of aliasing by using LRT to create 'desensitized' data, d_{kn}, from elastic earth synthetics, and then retrieving a model of apparent aspherical Q. Similar aliasing can result from the desensitizing method employed by Romanowicz (1990). We have demonstrated that employing the assumptions of LRT to remove the signal of elastic structure is, at any frequency, likely to be useful only as the first step in an iterative process, as argued by Durek *et al.* (1993).

By contrast, LRT describes fairly well the contribution from anelastic structure, over and above that of elastic structure, to surface wave amplitude anomalies for the first three or four Rayleigh wavepacket arrivals, and, like asymptotic theory for normal mode amplitudes, should be able to serve as a simplifying assumption to invert such data for models of aspherical anelastic structure, if an accurate *a priori* elastic model is assumed. However, to the extent that LRT holds, trends in odd and even index Rayleigh wavepacket arrivals are identical, so that the data would be insensitive to odd degree anelastic structure.

Departures from LRT, for the anelastic case, become significant for later surface wave arrivals, and seem largely attributable to surface wave path deviations expected to result from gradients of structure between source and receiver. These departures may supply additional information about aspherical structure. In particular, the odd and even index trends of $\ln(T_{e\to a}^{SW})$ become separated and, on average, path-averaged Q is depressed for multiply orbiting waves. Because both theory and observation indicate that odd and even orbits sample different structures on either side of the great circle, amplitude measurements for the

later wavepackets demonstrate some sensitivity to odd degree aspherical anelastic structure, as well as to gradients.

5 RESULTS AND CONCLUSIONS

The principal results from this study are as follows.

(1) Aspherical anelasticity accounts for at most 50 per cent, and more typically 30 per cent, of the average amplitude signal of long-wavelength elastic and anelastic aspherical earth structure, for long-period normal modes or surface wavepackets. The relative size of the anelastic signal is largest at the upper end of the frequency range considered, where the effects of unmodelled shorter wavelength elastic structure are expected to become significant, and in the case of surface wave amplitudes, anelastic effects are strongest for the later wavepackets, which are often not detectable in real data. Thus, though the effects of aspherical anelasticity in long-period data are surely significant enough to provide useful information about attenuative structure, in general more than half of the amplitude signal will be attributable to elastic structure, which must be taken into account when interpreting such data.

(2) Less than 1 per cent of the variance in the smoothed transfer functions $T_{RH\to a}^{NM}(l)$, which give the relative amplitude shifts of normal mode peaks due to elastic and anelastic aspherical structure, is accounted for by the zeroth-order equation for the anelastic amplitude effect, even though zeroth-order asymptotic theory predicts that any smooth trend in perturbations to normal mode amplitude spectra by aspherical earth structure results only from anelasticity. This is evidence that first- and higher order elastic effects are significant enough that simply removing the strong oscillating zeroth-order component of $T_{RH\to e}^{NM}(l)$ is insufficient to separate the elastic and anelastic amplitude signals in normal modes.

(3) Throughout the spectral range considered, surface wave amplitude data 'desensitized' to elastic structure using linearized ray theory (LRT) give values for path-averaged Q perturbations which are generally 50–100 per cent of the size of the maximum anelastic model perturbations, when synthetic data from a model with only elastic asphericities are used. This implies that deviations of surface waves away from great circle paths cause a breakdown of LRT significant enough to blur the distinction between elastic and anelastic surface wave amplitude effects forecast by that theory.

The preceding points demonstrate the necessity of employing phase data, which are practically insensitive to anelastic structure, to help determine elastic earth structure unambiguously, if long-period amplitude data are to be used to retrieve models of long-wavelength aspherical attenuative structure. The joint inversion of phase and amplitude data for elastic and anelastic structures, or the use of *a priori* elastic models derived from phase data (i.e. Durek *et al.* (1993), is recommended. Further results of this investigation indicate that the theoretical approximations considered may be useful for simplifying the inversion for aspherical anelasticity.

(1) Fifty-five per cent of the variance of the unsmoothed transfer functions $T^{NM}_{e \to a}(l)$ and about 85 per cent of the smoothed function variance is accounted for by zeroth-order asymptotic theory for anelastic structure, where $T^{NM}_{e \to a}(l)$ maps peak amplitudes of normal mode spectra of an elastic earth model to those of a model including anelasticity. This suggests that, given an *a priori* elastic model and a sufficiently sophisticated smoothing algorithm, zeroth-order asymptotic theory may be useful for simplifying the inversion of $T^{NM}_{e \to a}(l)$ for long-period aspherical anelastic structure. However, the success of asymptotic theory in predicting synthetic trends also indicates that normal mode amplitude data may prove insensitive to odd-order anelastic structure.

(2) Slopes for $\ln[T^{SW}_{e \to a}(n)]$ predicted by LRT account for up to 67 per cent of the variance of measured slopes for the synthetics, for wavepackets R1–R3. For each frequency, $T^{SW}_{e \to a}(n)$ maps the Rayleigh wavepacket amplitudes for an elastic earth to those of a model with aspherical anelasticity, as a function of orbit index. Trends are observed to be nearly linear for these first few arrivals. Together these results indicate that the LRT approximation may be appropriate for interpreting $T^{SW}_{e \to a}(n)$ for R1–R3, but this simplification results in insensitivity to odd degree anelastic structure.

(3) LRT is less successful in predicting $\ln[T^{SW}_{e \to a}(n)]$ trends for R1–R8, giving approximately 50 per cent variance reductions. Path wander due to bending of ray paths by elastic structure appears to be responsible. The departure from LRT gives such data some sensitivity to odd degree aspherical anelastic structure.

It must be emphasized that all of the above results and conclusions apply to long-wavelength aspherical models. The effects of shorter wavelength structures are likely to modify these results. In the future, it will be possible to add realistic models of such structures, to include Love waves in the investigation, to test quantitatively the effectiveness of the first-order (in $(1/l)$) terms of the asymptotic theory in approximating anelastic amplitude perturbations, and to model the path wander of surface waves.

REFERENCES

Dahlen, F.A., 1987. Multiplet coupling and the calculation of synthetic long-period seismograms, *Geophys. J. R. astr. Soc.*, **91**, 241–254.

Davis, J.P., 1985. Variation in apparent attenuation of the Earth's normal modes due to lateral heterogeneity, *Geophys. Res. Lett.*, **12**, 141–143.

Davis, J.P., 1987. Local eigenfrequency and its uncertainty inferred from spheroidal mode frequency shifts, *Geophys. J. R. astr. Soc.*, **88**, 693–722.

Davis, J.P. & Henson, I.H., 1986. Validity of the great circle average approximation for inversion of normal mode measurements, *Geophys. J. R. astr. Soc.*, **85**, 69–92.

Durek, J.J., Ritzwoller, M.H. & Woodhouse, J.H., 1993. Constraining upper mantle anelasticity using surface wave amplitude anomalies, *Geophys. J. Int.*, **114**, 249–278.

Dziewonski, A.M., 1984. Mapping the lower mantle: Determination of lateral heterogeneity in *P* velocity up to degree and order 6, *J. geophys. Res.*, **89**, 5929–5952.

Dziewonski, A.M. & Anderson, D.L., 1981. Preliminary Reference Earth Model, *Phys. Earth planet. Inter.*, **25**, 297–356.

Jobert, N. & Roult, G., 1976. Periods and damping of free oscillations observed in France after sixteen earthquakes, *Geophys. J. R. astr. Soc.*, **45**, 155–176.

Jordan, T.H., 1978. A procedure for estimating lateral variations from low-frequency eigenspectra data, *Geophys. J.R. astr. Soc.*, **52**, 441–455.

Lognonné, P., 1991. Normal modes and seismograms in an anelastic rotating earth, *J. geophys. Res.*, **96**, 20 309–20 319.

Masters, G., 1989. Seismic modelling of the Earth's large-scale three-dimensional structure, *Phil. Trans. R. Soc. Lond.*, A, **328**, 329–349.

Masters, G., Bolton, H. & Shearer, P., 1992. Large-scale 3-dimensional structure of the mantle, *EOS, Trans. Am. geophys. Un.*, **73**, 20.

Masters, G., Jordan, T.H., Silver, P.G. & Gilbert, F., 1982. Aspherical earth structure from fundamental spheroidal mode data, *Nature*, **298**, 609–613.

Montagner, J.-P. & Tanimoto, T., 1991. Global upper mantle tomography of seismic velocities and anisotropies, *J. geophys. Res.*, **96**, 20 337–20 351.

Nakanishi, I. & Anderson, D.L., 1982. Worldwide distribution of group velocity of mantle Rayleigh waves as determined by spherical harmonic inversion, *Bull. seism. Soc. Am.*, **72**, 1185–1194.

Nakanishi, I. & Anderson, D.L., 1983. Measrurement of mantle wave velocities and inversion for lateral heterogeneity and anisotropy, I. Analysis of great circle phase velocities, *J. geophys. Res.*, **88**, 10 267–10 283.

Nakanishi, I. & Anderson, D.L., 1984. Measurement of mantle wave velocities and inversion for lateral heterogeneity and anisotropy, II. Analysis by the single station method, *Geophys. J. R. astr. Soc.*, **78**, 573–618.

Nataf, H.-C., Nakanishi, I. & Anderson, D.L., 1984. Anisotropy and shear velocity heterogeneities in the upper mantle, *Geophys. Res. Lett.*, **11**, 109–112.

Nataf, H.-C., Nakanishi, I. & Anderson, D.L., 1986. Measurement of mantle wave velocities and inversion for lateral heterogeneity and anisotropy, III. Inversion, *J. geophys. Res.*, **91**, 7261–7307.

Park, J., 1986. Synthetic seismograms from coupled free oscillations: Effects of lateral structure and rotation, *J. geophys. Res.*, **91**, 6441–6464.

Park, J., 1987. Asymptotic coupled-mode expressions for multiplet amplitude anomalies and frequency shifts on an aspherical Earth, *Geophys. J. R. astr. Soc.*, **90**, 129–169.

Park, J. & Yu, Y., 1992. Anisotropy and coupled free oscillations: Simplified models and surface wave observations, *Geophys. J. Int.*, **110**, 401–420.

Pollitz, F.F., Park, J. & Dahlen, F.A., 1987. Observations of free oscillation amplitude anomalies, *Geophys. Res. Lett.*, **91**, 7241–7260.

Ritzwoller, M.H., Durek, J.J. & Woodhouse, J.H., 1989. Inferences from measurements of aspherical *Q*, *EOS, Trans. Am. geophys. Un.*, **70**, 1212.

Romanowicz, B., 1987. Multiplet–multiplet coupling due to lateral heterogeneity: asymptotic effects on the amplitude and frequency of the Earth's normal modes, *Geophys. J. R. astr. Soc.*, **90**, 75–100.

Romanowicz, B., 1990. The upper mantle degree 2: Constraints and inferences from global mantle wave attenuation measurements, *J. geophys. Res.*, **95**, 11 051–11 071.

Romanowicz, B., 1991. Seismic tomography of the Earth's mantle, *Ann. Rev. Earth planet. Sci.*, **19**, 77–90.

Romanowicz, B. & Roult, G., 1986. First-order asymptotics for the eigenfrequencies of the Earth and application to the retrieval of large-scale lateral variations of structure, *Geophys. J. R. astr. Soc.*, **87**, 209–239.

Romanowicz, B., Roult, G. & Kohl, T., 1987. The upper mantle degree two pattern: Constraints from Geoscope Fundamental spheroidal mode eigenfrequency and attenuation measurements, *Geophys. Res. Lett.*, **14**, 1219–1222.

Sato, H., Sacks, I.S. & Murase, T., 1989. The use of laboratory velocity data for estimating temperature and partial melt fraction in the low-velocity zone: comparison with heat flow and electrical conductivity studies, *J. geophys. Res.*, **94**, 5689–5704.

Sato, H., Sacks, I.S., Murase, T., Muncill, G. & Fukuyama, H., 1989. *Qp*–melting temperature relation in peridotite at high pressure and temperature: Attenuation mechanism and implications for the mechanical properties of the upper mantle, *J. geophys. Res.*, **94**, 10 647–10 661.

Smith, M.F. & Masters, G., 1989. Aspherical structure constraints from normal mode frequency and attenuation measurements, *J. geophys. Res.*, **94**, 1953–1976.

Snieder, R., 1986. 3-D linearized scattering of surface waves and a formalism for surface wave holography, *Geophys. J. R. astr. Soc.*, **84**, 581–605.

Su, Wei-jia, Woodward, R.L. & Dziewonski, A.M., 1993. Degree-12 model of shear velocity heterogeneity in the mantle, *J. geophys. Res.*, submitted.

Tanimoto, T., 1986. The Backus–Gilbert approach to the three-dimensional structure in the upper mantle, II. *SH* and *SV* velocity, *Geophys. J. R. astr. Soc.*, **84**, 49–70.

Tanimoto, T. & Anderson, D.L., 1984. Mapping convection in the mantle, *Geophys. Res. Lett.*, **11**, 287–290 (1984).

Tanimoto, T. & Anderson, D.L., 1985. Lateral heterogeneity and azimuthal anisotropy of the upper mantle: Love and Rayleigh waves 100–250s, *J. geophys.*, **90**, 1842–1858.

Tromp, J. & Dahlen, F.A., 1990. Free oscillation of a spherical anelastic Earth, *Geophys. J. Int.*, **103**, 707–723.

Um, J., Dahlen, F.A. & Park, J., 1991. Normal mode multiplet coupling along a dispersion branch, *Geophys. J. Int.*, **106**, 11–35.

Wong, Y.K., 1989. Upper mantle heterogeneity from phase and amplitude data of mantle waves, *PhD thesis*, Harvard University, Cambridge.

Woodhouse, J.H., 1980. The coupling and attenuation of nearly resonant multiplets in the earth's free oscillation spectrum, *Geophys. J. R. astr. Soc.*, **61**, 261–283.

Woodhouse, J.H. & Girnius, T.P., 1982. Surface waves and free oscillations in a regionalized Earth model, *Geophys. J. R. astr. Soc.*, **68**, 653–673.

Woodhouse, J.H. & Dziewonski, A.M., 1984. Mapping the upper mantle: Three dimensional modeling of Earth structure by inversion of seismic waveforms, *J. geophys. Res.*, **89**, 5953–5986.

Woodhouse, J.H. & Wong, Y.K., 1986. Amplitude, phase and path anomalies of mantle waves, *Geophys. J. R. astr. Soc.*, **87**, 753–773.

Yu, Y. & Park, J., 1993. Upper mantle anisotropy and coupled-mode long-period surface waves, *Geophys. J. Int.*, **114**, 473–489.

APPENDIX

A Asymptotic normal mode theory

The approximate equations for a seismogram derived by Romanowicz (1987) can easily be generalized to include attenuation. The asymptotics that result provide descriptions, correct up to first order in $(1/l)$, of how both elastic and anelastic aspherical structure perturb the amplitudes and phases of the fundamental branch normal mode multiplets of a rotating hydrostatic earth.

The Born approximation for a seismogram at time t and angular distance Δ from the source is:

$$s(t, \Delta) = \mathscr{R}e \left[\sum_K \mathscr{A}_K \exp\left(-\alpha_K t\right) \exp\left(i\omega_K t\right) \right], \tag{A1}$$

where K corresponds to the radial and angular indices, (n, l), of the multiplet with degenerate frequency ω_K. The attenuation factor α_K is related to the degenerate Q of the multiplet by $\alpha_K = \omega_K/2Q_K = \omega_K q_K/2$.

For the SNRI model and in the case of an isotropic source,

$$\mathscr{A}_K = \mathscr{A}_K^0 = M_0 \frac{\alpha_{kk}}{\pi\sqrt{\sin \Delta}} \sqrt{\frac{k}{2\pi}} \cos\left(k\Delta - \frac{\pi}{4} - \frac{\cot \Delta}{8k}\right). \tag{A2}$$

M_0 is the scalar moment of the source, $k = l + 1/2$, and α_{kk} is a function of the vertical eigenfunctions of the reference model. For a model that includes elastic and anelastic asphericities, and again for an isotropic source,

$$\mathscr{A}_K = a_k[\mathscr{G}_1(\Delta) \cos(k\Delta - \pi/4) + \mathscr{G}_2(\Delta) \sin(k\Delta - \pi/4)], \tag{A3}$$

where

$$a_k = M_0 \frac{\alpha_{kk}}{\pi\sqrt{\sin \Delta}} \sqrt{\frac{k}{2\pi}}, \tag{A4}$$

$$\mathscr{G}_1(\Delta) = 1 + \frac{a\Delta}{U}\left[\left(\frac{\hat{\mathscr{D}}_k - \tilde{\mathscr{D}}_k}{2k}\right) + \frac{\cot \Delta}{8k}(\delta\hat{\sigma}_k - \delta\tilde{\sigma}_k)\right] + it\,\delta\hat{\sigma}_k, \tag{A5}$$

$$\mathscr{G}_2(\Delta) = \frac{\cot \Delta}{8k} - \frac{a\Delta}{U}(\delta\hat{\sigma}_k - \delta\tilde{\sigma}_k) + it\left(\frac{\hat{\mathscr{D}}_k}{2k} + \frac{\cot \Delta}{8k}\delta\hat{\sigma}_k\right). \tag{A6}$$

In the above, a is the radius of the Earth, and U is the group velocity at frequency ω_k. We have also used the definitions

$$\delta\hat{\sigma}_k = \frac{1}{2\pi}\int_0^{2\pi} \delta\sigma_k^0(s)\,ds, \tag{A7}$$

$$\delta\tilde{\sigma}_k = \frac{1}{\Delta}\int_0^{\Delta} \delta\sigma_k^0(s)\,ds, \tag{A8}$$

$$\hat{\mathscr{D}}_k = \frac{1}{2\pi}\int_0^{2\pi} \mathscr{D}_k(\phi)\,d\phi, \tag{A9}$$

$$\tilde{\mathscr{D}}_k = \frac{1}{\Delta}\int_0^{\Delta} \mathscr{D}_k(\phi)\,d\phi, \tag{A10}$$

where the integrals are along the source to receiver great circle. $\mathscr{D}$ is defined by

$$\mathscr{D}_k = \frac{\sin(\phi - \Delta)}{\sin \Delta}[\partial_\theta^2(\delta\sigma_k^0)\sin \phi - \partial_\phi(\delta\sigma_k^0)\cos \phi], \tag{A11}$$

and $\delta\sigma_k^0$ is the generalization of the local frequency (Jordan 1978; Woodhouse & Girnius 1982) to include attenuation:

$$\delta\sigma_k^0 = \delta\omega_k^0 + i\,\delta\alpha_k^0 = \delta\omega_k^0 + i\frac{\omega_k}{2}\,\delta q_k^0. \tag{A12}$$

If σ is replaced by ω, the above relations become identical to eqs (1), (38), (44), (45), (47), (57) and (58) of Romanowicz (1987).

If we consider now just the contributions to eq. (A3) from the SNRI model and aspherical elastic structure, reducing $\delta\sigma_k$ to $\delta\omega_k$ and $\mathcal{D}_k$ to $D_k = \mathcal{R}e\,[\mathcal{D}_k]$, we can rewrite eq. (A1) as:

$$s(t, \Delta) = \mathcal{R}e\left\{\sum_k a_k(A_{0k} + \delta\mathcal{A}_k)\exp\left(-\alpha_k t\right)\right.$$

$$\left. \times \exp\left[i(\omega_k + \Lambda_k)t\right]\right\}, \tag{A13}$$

with

$$A_{0k} = \cos\lambda_k + \frac{\cot\Delta}{8k}\sin\lambda_k, \tag{A14}$$

$$\delta A_k = \frac{a\Delta}{U}\left[\left(\frac{\bar{D}_k}{2k} + \frac{\cot\Delta}{8k}\overline{\delta\omega_k}\right)\cos\lambda_k - \overline{\delta\omega_k}\sin\lambda_k\right], \tag{A15}$$

$$\Lambda_k = \delta\hat{\omega}_k + \frac{\hat{D}_k}{2k}\tan\lambda_k. \tag{A16}$$

The abbreviations $\lambda_k = k\Delta - (\pi/4)$, $\bar{D}_k = \hat{D}_k - \check{D}_k$ and $\overline{\delta\omega_k} = \delta\hat{\omega}_k - \delta\check{\omega}_k$ have been used. The summation has been restricted to the fundamental branch, and the expressions for amplitude and frequency are, for short times, correct to first order in $(1/l)$. Note that the zeroth-order term of the multiplet frequency shift Λ_k is just the path-averaged local frequency $\delta\hat{\omega}$ of the geometrical optics approximation for self-coupling.

The relative amplitude shift is

$$\frac{\delta A_k}{A_{0k}} = \frac{a\Delta}{U}\left(-\overline{\delta\omega_k}\tan\lambda + \frac{\bar{D}_k}{2k} + \frac{\cot\Delta}{8k}\overline{\delta\omega_k}\sec^2\lambda\right). \tag{A17}$$

The spectrum produced by the Fourier transform of eq. (A13) will have multiplets with amplitudes shifted from their SNRI values according to eq. (A17). The frequencies of the perturbed multiplets will be shifted by the amounts given in eq. (A16), but the change in frequency will also alter the phase of the multiplet as measured at the location of the unperturbed multiplet ($\omega = \omega_k$). For a time series of length T satisfying the short-time approximation, $\Lambda_k T \ll 1$, and thus consistent with the Born approximation, this phase shift will be

$$\psi_k^{(\text{clas})} = -\frac{\Lambda_k}{\alpha_k}. \tag{A18}$$

Including the anelastic model perturbations changes the displacement equation to

$$s(t, \Delta) = \mathcal{R}e\left[\sum_k a_k(A_{0k} + \delta A_k)\exp\left[-(\alpha_k + \delta\alpha_k)t\right]\right.$$

$$\left. \times \exp\left\{i[(\omega_k + \Lambda_k)t + \psi_k^{\text{anel}}]\right\}\right], \tag{A19}$$

where, with $d_k = \mathcal{I}m\,[\mathcal{D}_k]$,

$$\delta\alpha_k = \delta\hat{\alpha}_k + \frac{\hat{d}_k}{2k}\tan\lambda_k, \tag{A20}$$

$$\psi_k^{(\text{anel})} = \frac{a\Delta}{U}\left(-\overline{\delta\alpha_k}\tan\lambda_k + \frac{\bar{d}_k}{2k} + \frac{\cot\Delta}{8k}\overline{\delta\alpha_k}\,s^2\,\lambda_k\right). \tag{A21}$$

When the spectrum for the seismogram of eq. (A19) is compared with that of eq. (A13), the observed phase shift is given by eq. (A21). Amplitudes for an infinite time series go as $1/\alpha$, so that amplitude perturbations are given by

$$\frac{A_k^{(\text{anel})}}{A_k^{(\text{elas})}} = 1 - \frac{\delta\alpha_k}{\alpha_k}. \tag{A22}$$

If we consider only the zeroth order in $(1/l)$, so that $\delta\alpha_k = \delta\hat{\alpha}_k$, and define a great circle average of aspherical Q by perturbing the relation $Q_k = \omega_k/2\alpha_k$:

$$\frac{\delta\hat{Q}_k}{Q_k} = -\frac{\delta\hat{\alpha}_k}{\alpha_k}. \tag{A23}$$

Eq. (A22) then becomes

$$\frac{A_k^{(\text{anel})}}{A_k^{(\text{elas})}} = 1 + \frac{\delta\hat{Q}_k}{Q_k}. \tag{A24}$$

If we use a time series of length T, subjected to a Hanning taper,

$$\frac{1}{2}\left(1 - \cos\frac{2}{T}\right), \tag{A25}$$

then peak amplitudes go as

$$[1 - \exp\left(-\alpha T\right)]\left(\frac{1}{\alpha}\right)\left(\frac{\beta^2}{\alpha^2 + \beta^2}\right), \tag{A26}$$

with $\beta = 2\pi/T$. For this case, eq. (A22) becomes

$$\frac{A_k^{(\text{anel})}}{A_k^{(\text{elas})}} = 1 - \frac{\delta\alpha_k}{\alpha_k}\left[\gamma + \frac{\alpha T}{\exp\left(\alpha T\right) - 1}\right], \tag{A27}$$

where $\gamma = (\beta^2 + 3\alpha^2)/(\beta^2 + \alpha^2)$ and eq. (A24) changes accordingly.

Equation (A20) comes from the time-dependent part of the real amplitude of expression eq. (A3), under the assumption that $A_{0k} = \cos\lambda_k + \dfrac{\cot\Delta}{8k}\sin\lambda_k$ gives amplitudes much greater than the size of the amplitude perturbations. This is not the case near a node of the SNRI model. Backing up one step in the derivation of eq. (A20), we have:

$$\delta\alpha_k = \frac{\delta\hat{\alpha}_k}{\cos\lambda_k}A_{0k} + \left(\frac{\hat{d}_k}{2k} - \frac{\cot\Delta}{8k}\delta\hat{\sigma}_k\right)\tan\lambda_k. \tag{A28}$$

If we are not at a node, these terms combine to give eq. (A20). At nodes the magnitude of A_{0k} is of the same order as $\delta\hat{\alpha}_k$, and the first term on the right in eq. (A28) is second order in the perturbation, and may be treated as vanishing. The remaining terms produce a function that oscillates about zero, rather than about $\delta\hat{\alpha}_k$, with a first-order amplitude that depends on both $\delta\hat{\alpha}_k$ and $\hat{d}_k$, rather than just the latter.

It also should be noted that though we have, for the sake of clarity, presented only the equations for an isotropic

source, the introduction of realistic moment tensors does not significantly alter the relevant characteristics of eqs (A20) and (A28). Generalizing eq. (78) of Romanowicz (1987) for anelasticity, shows that the effect of a moment tensor source is to add another first-order gradient term to $\frac{\hat{d}_k}{2k}$. Also, the mathematical work of Romanowicz & Roult (1986), indicates that the results for the longitudinal horizontal component will differ only slightly from those for the vertical component, while the transverse component will lack the zeroth-order local frequency and attenuation terms, but remain similar in the first-order terms.

B Linearized ray theory

A second way to view the effects of anelastic aspherical structure on synthetic seismograms is as amplitude and phase perturbations of surface waves. We consider here, in particular, the sequence of wavepackets R_1–R_8.

For the elastic case, Fermat's principle gives for the phase shift of R_n:

$$\delta\psi_n = -\frac{\omega a}{c_0}\int_0^{\Delta n}\frac{\delta c(\theta, \phi)}{c_0}\,d\phi, \tag{B1}$$

where c is phase velocity and Δ_n is the angular distance along the great circle $\theta = \pi/2$ travelled by R_n. This implies that

$$\delta\psi_n = \begin{cases} -\omega a c_0^{-1}[I_1 + \frac{1}{2}(n-1)I_2] & (n\text{ odd}) \\ -\omega a c_0^{-1}[-I_1 + \frac{1}{2}nI_2] & (n\text{ even}) \end{cases}, \tag{B2}$$

where I_1 is the integral of eq. (B1) along the source–receiver minor arc and I_2 that around the whole great circle. Thus, the phase shifts as functions of orbit number form two parallel lines.

Woodhouse & Wong (1986) have shown that a similar relationship holds for the amplitude anomalies:

$$\ln\left(\frac{\delta A}{A}\right)_n = \begin{cases} \frac{1}{2}csc\,\Delta[J_1 + \frac{1}{2}(n-1)J_2] & (n\text{ odd}) \\ \frac{1}{2}csc\,\Delta[J_1 - \frac{1}{2}nJ_2] & (n\text{ even}) \end{cases}. \tag{B3}$$

Here, J_1 and J_2 are the minor arc and great circle integrals of a function that depends on the second transverse derivative of phase velocity along the path:

$$J = \int_0^\Delta \sin(\Delta - \phi)c_0^{-1}[\sin\phi\,\partial_\theta^2 - \cos\phi\,\partial_\phi]\delta c\,d\phi. \tag{B4}$$

In this approximation, therefore, the amplitude anomalies of even and odd index wavepackets should form two lines with opposite slopes.

The attenuation term in eq. (A19) results in a simple modification of the surface wave amplitudes. Let us abbreviate, for the moment, $(\delta A/A)_n$ as a_n. If the slopes of the surface wave trends of eq. (B23) are $\pm\gamma = \frac{1}{2}(\ln a_{n+2} - \ln a_n)$, so that in the elastic case we have $a_{n+2} = a_n\exp(\pm2\gamma)$, then when anelastic structure is included we have $a_{n+2} = a_n\exp(\pm2\gamma)\exp[-\delta\alpha(\Delta t)]$. Since the time for one orbit is approximately $\Delta t = 2\pi a/u_0$ for group velocity u_0, we can write:

$$\left(\frac{A_k'}{A_k^0}\right)_{n+2} = \left(\frac{A_k'}{A_k^0}\right)_n \exp(\pm2\gamma_k)\exp\left(\frac{-2\pi a}{u_k}\delta\alpha_k\right). \tag{B5}$$

This is a relation for the total amplitude shift for elastic and anelastic structure and implies that the slope in the logarithmic plot has changed to $\pm\gamma + \left(\frac{-\pi a}{u_k}\delta\alpha_k\right)$. This shift applies to both the even and odd index trends. If we display in the same manner just the relative perturbation introduced by anelastic attenuation, the even and odd index trends will be colinear, with a slope of simply:

$$\gamma_k' = -\frac{\pi a}{u_k}\delta\alpha_k = \frac{\pi a}{u_k}\frac{\omega_k}{2Q_k}\left(\frac{\delta\hat{Q}_k}{Q_k}\right), \tag{B6}$$

for surface waves at the frequency of the fundamental branch multiplet indexed by k. The last equality assumes the zeroth-order approximation of eq. (A23).